Energetics of reaction pathways enabled by N and H radicals during catalytic, plasma-assisted NH3 synthesis

Tsung-Wei Liu,[a] Fnu Gorky [b], Maria L. Carreon,[c] Diego A. Gómez-Gualdrón[a] *

[a] Department of Chemical and Biological Engineering, Colorado School of Mines, Golden CO 80401, USA

[b] Department of Chemical Engineering, South Dakota School of Mines, Rapid City SD 57701, USA

[c] Department of Mechanical Engineering, University of Massachusetts-Lowell, Lowell MA 01854, USA

ABSTRACT: Plasma-assisted catalysis is emerging as an alternative to several thermocatalytic processes. For ammonia synthesis, it could make the process milder, which would help production, decentralization and compatibility with renewable energy. However, one major obstacle preventing optimization of the plasma-assisted process is the incipient mechanistic understanding of ammonia formation on plasma-exposed catalysts. Here, optical emission spectroscopy OES is consistent with only a weak effect of the metal on plasma composition, and with the presence of small concentrations of plasma radicals in N_2/H_2 mixtures in DBD reactors, which are bound to enable new catalyst-involved pathways not considered in previous kinetic models for NH_3 synthesis. Thus, we comprehensively examined, via density functional theory (DFT) calculations, the energetics (favorability) of 51 reactions on Fe, Ni, Co, Pd, Ga, Sn, Cu, Au, and Ag. Enthalpic barriers for Eley-Rideal (ER) reactions involving N• and H• radicals were found to be negligible and hence supportive of: *i)* plausible NNH formation and consequent prominent role of the associative pathway to form NH_3 (consistent with some experimental reports detecting surface-bound N_XH_Y species), *ii)* likelihood of N• adsorption taking over N_2* dissociation as the primary source of surface bound N*, and iii) probable dominance of ER hydrogenation reactions over Langmuir-Hinshelwood (LH) ones. The energetics herein presented will allow thoroughly studying pathway competition in future kinetic models, but numbers calculated here already suggest that the dominant pathway may change with metal identity. For instance, N_2H_Y dissociation favorability is more likely to become competitive with ER hydrogenation earlier in the hydrogenation sequence in the more nitrophilic the metals. Yet, the calculated favorability of ER reactions is also already consistent with the weaker dependence of initial NH_3 turnover frequencies (TOFs) on metal identity compared to the thermocatalytic scenario. With practical implications for computational catalyst screening, TOFs experimentally measured herein for an atmospheric dielectric barrier discharge (DBD) reactor linearly correlate with ΔE_{rxn} for the ER hydrogenation reaction $H• + HNNH_2* \rightarrow HNNH_3*$. This descriptor may be robust to exact synthesis conditions, as its correlation with TOFs was maintained for earlier TOF data in a sub-atmospheric radio frequency (RF) reactor.

■ INTRODUCTION

Ammonia is a crucial chemical due to its widespread use in fertilizer production[1] and could gain further importance in the future as a hydrogen carrier[2] in a so-called "hydrogen economy."[3] The current yearly demand for ammonia is more than 200 million tons,[4] with ammonia primarily produced from H_2/N_2 mixtures using a thermocatalytic process known as Haber Bosch (HB).[5] HB requires high temperature to break the N≡N bonds in N_2, high pressure to alleviate temperature-driven reaction equilibrium limitations and, due to the high pressure, centralized ammonia production to make the process economically feasible. Currently, HB plants demands ca. 2% of the world's energy[6]—greatly due to the required *in situ* H_2 generation via CH_4 reforming to feed the process—and is responsible for ca. 1 % of the world's CO_2 emissions.[6] An opportunity to address the need to "decarbonize" ammonia production is through the use of decentralized "green" hydrogen, which also has the appeal of decentralizing ammonia production (e.g., it could be produced *in situ* in farms using it for fertilizers). However, as green hydrogen is likely to be intermittent in nature, compatible ammonia synthesis processes need to be easily turned "on and off" for on-demand production. Given that the harsh HB conditions are incompatible with the above scenario,[7] it is critical to develop methods to synthesize ammonia under mild conditions.[7–10]

A way towards mild ammonia synthesis is to help the catalyst break N≡N bonds at reasonable rates at moderate reactor temperature. A potential way to achieve this is by "electrifying" the process using electric fields,[11] electrochemistry[12] or plasmas,[13] where the electricity could come from, for instance, solar or wind energy (the same sources that would be used to produce the green hydrogen feed).[14,15] In plasma reactors, electrical power would be used to generate a plasma phase where electron collisions with N_2 and H_2 can excite and/or dissociate molecular species. Even without a catalyst, the plasma excitation/dissociation products can

collide with electrons and/or react with each other in a complex reaction network[16] that ultimately leads to the formation of some NH_3—and some N_2H_2 depending on the reaction conditions (e.g., the type of plasma).[17–19] However, some authors suggest that most of ammonia formation in "catalyst-less" plasma reactors occurs at the reactor walls instead of the bulk plasma,[16] probably by adsorptive concentration of plasma species on the wall surface.

On the other hand, the introduction of a metal catalyst into the reactor often increases ammonia production by several-fold,[20] indicating that under a plasma environment a "proper" catalyst likely does more than concentrate reactive species. The issue is that the "controlling" reaction pathways and the exact role of the catalyst under plasma conditions remain unclear and under debate, primarily due to the aforementioned high complexity of plasma reaction networks.[21] This complexity also makes effects such as plasma-catalyst synergy difficult to unravel, at least to the extent needed to be predictive and able to rationally design better catalysts that can improve current ammonia energy-yields in plasma reactors (current record is 36 g-NH_3/kWh)[22] to more competitive values (100-200 g-NH_3/kWh).

Some aspects of plasma-assisted ammonia synthesis on metal catalysts are increasingly clear from experiments. These include: *i)* the non-Arrhenius dependence of NH_3 formation rates on temperature as reported by both Hicks and coworkers[23] and Lefferts and coworkers[24], *ii)* the ability to reach conversions beyond the thermal equilibrium limit also reported by both above teams in separate works[25,26] and *iii)* the first and zeroth dependence of NH_3 formation rates on N_2 and H_2 pressure respectively, as determined by Hicks and coworkers[23] from careful kinetic experiment at differential reactor conditions. However, these experiments are inconclusive on (among other mechanistic aspects) a crucial debate point: whether vibrationally excited species or radical species are the species involved in the "rate controlling" steps to produce ammonia, particularly in dielectric barrier discharge (DBD) reactors. Accordingly, computational work is called to complement experiments to shed some light on the mechanistic debate.

The case for vibrationally excited $N_2(v)$ stems from their expected abundance at typical electron temperatures for DBD reactors, and its enhanced dissociation rates to produce N* (* = catalyst site) relative to regular N_2, which could explain enhanced catalytic NH_3 production rates under plasmas. Schneider and coworkers[27] postulated that the dissociation rate enhancement for $N_2(v)$ can be quantified by the a reduction in the dissociation barrier by nhv quanta, where n = excitation level, h =plank constant, v= vibration frequency. These authors thus implemented this idea into a microkinetic model, where the catalyst was exposed to a "minimal plasma" phase that included $N_2(v)$ but excluded plasma radicals. Accordingly, $N_2(v)$ dissociative adsorption was the only "extra" reaction in the model besides the traditional HB reactions.

On the other hand, radicals *are* expected to form in DBD plasmas. Using optical emission spectroscopy (OES), Wang *et al*[28]. reported both N• and H• plasma radicals during catalytic ammonia synthesis in a DBD reactor. The difficulty in forming N• is the required collision of N_2 with electrons of energy 9.6 eV, but even these energies can be found (albeit as minority) at the tail of the electron energy distribution at typical electron temperatures. Authors such as Lefferts and coworkers [25] also argue that the catalyst-free formation of NH_3 under DBD plasmas is another (indirect) indication of the formation of plasmas radicals. The key here is that, due to their high reactivity, only a small concentration of radicals *could* let them "take over" the reaction mechanism. For instance, even a small fraction of N• radicals reaching the catalyst surface *could* outcompete N_2 (and $N_2(v)$) dissociation as a source of N* and thus *could* also explain enhanced catalytic NH_3 formation rates under plasmas.

Importantly, the involvement of radicals on NH_3 formation on the catalyst could also produce changes beyond rate enhancement. Radicals reaching the catalyst surface could, for instance, enable Eley-Rideal (ER) reactions with surface species. Indeed, the occurrence of ER reactions between plasma radicals and chemisorbed species is suggested by isotopic labeling experiments by Gomez-Ramirez and coworkers.[29] Although the case built by these experiments, is stronger for ER reactions involving NH_x• radicals created from NH_3 decomposition, and more speculative for N• and H• radicals created before NH_3 is formed. Intriguingly, using FTIR spectrometry, Chen and coworkers[30] reported the detection of N_2H_Y on metal surfaces during catalytic NH_3 synthesis under DBD plasmas, whereas, Koel and cowokers[31] reported the detection of NNH and N_2H_2 using molecular beam mass spectrometry. It is unclear how surface N_2H_Y could form if only $N_2(v)$ (and not radicals) reach the catalyst surface, so the presence of N_2H_Y species could be an indication of the direct mechanistic involvement of N• and H• on catalytic NH_3 formation via ER reactions (a point of discussion in the present work).

Partly motivated by the above, interest on fundamentally understanding the role of plasma radicals on reactions at the catalyst surface continues to increase. Recently, Mangolini and coworkers[32] used *ab initio* molecular dynamics (AIMD) to study the few picoseconds following the impingement of an N• radical on Cu and Pt surfaces fully covered with H*. In their simulations, N• seemed to more easily abstract H* from Cu than from Pt to form NH_3, which the authors explained based on the stronger binding of N* in Pt. However, NH_3 formation in their RF plasma experiments was actually more efficient in Pt than Cu. This apparent discrepancy could be due to incorrect assumptions about H* coverage and/or limiting the simulation to the one "reaction event" of N• impingement on a H-covered surface. The "time limitations" of AIMD underscore the complementary value of kinetic models that can account for the variety of reactions that can happen involving plasma and surface-bound species at larger time scales. These models would allow understanding how the different reactions proceed on different metal catalysts, and how the catalyst state changes under different plasma conditions (as there are some differences in reaction conditions among reported experiments). However, to be reliable, these models need to be "complete" (e.g., include all relevant reactions) and use sufficiently accurate enough reaction parameters.

Several authors[33–35] have used detailed "zero-dimensional" kinetic models including both reactions in the plasma and on a catalyst, aiming to understand catalytic NH_3 formation under plasmas. For instance, both Murphy and coworkers[34] and Boegaerts and coworkers[33] lent further support to the presence of N• and H• (and other) radicals in DBD plasmas, although they disagreed on the influence of these radicals on the reactions involving the catalyst, what the ammonia formation rate controlling step was, as well as other mechanistic aspects. Disagreements aside, it is worth noting that several key reactions parameters in their models were obtained from empirical fitting, hence presented uncertain accuracy. Perhaps, this is more noticeable for reactions involving the catalyst. For instance, Boegaerts and coworkers[33] noted the conflict between plasma literature parameters intended to represent reactions on Fe and the corresponding known parameters from density functional theory (DFT) calculations. Using accurate parameters for reactions involving the catalyst, however, is especially important in a scenario where the strategy to validate kinetics models (and related mechanistic insights) would rely on capturing experimental trends across different catalysts (e.g., NH_3 rate of formation trends).

Accordingly, recognizing on one hand the tremendous potential of kinetic models to provide mechanistic information to a level of detail not accessible by experiments, but on the other hand the crucial need for model completeness and parameter accuracy, in the present work we aimed to use (DFT) calculations to obtain the energetic information that would yield first principles-informed reaction parameters for a (potentially) complete plasma-catalyst model. Accordingly, we set out to interrogate with DFT *i)* the adsorption energetics of "gas" N_XH_Y species (X = 0-2, Y = 0-3), *ii)* the energetics of LH reactions involving surface N_XH_Y* species, and *iii)* the energetics of ER reactions involving N_XH_Y* surface species and H• and N• radicals, and *iv)* the energetics of dissolution of N* and H* to subsurface sites. While calculations *i* through *iii* are motivated by the earlier noted plausible involvement of plasma radicals on reactions at the catalyst surface, as well as surface N_2H_Y* (and thus the involvement of the so-called associative mechanism pathway), calculation *iv* is motivated by our previous RF reactor experiments.[20] These experiments suggested that H* dissolution (through a "hydrogen sink" effect) and N* dissolution (as a precursor step to nitride formation) could impact ammonia formation rates.

To choose the catalysts for our calculations, we considered metals for which experimental trends for NH_3 formation rates were available, as this way the implementation of our parameters in future models could lend itself for model validation against experimental trends. For instance, in our RF experiments,[20] we observed NH_3 formation rates to follow the trend Au > Sn > Ag > Ni > Pd > Cu > Ga > Fe, whilst Iwamoto and coworkers[36] reported NH_3 formation rates in DBD experiments to follow the trend Au > Pt > Pd > Ag > Cu > Fe > Ni. Accordingly, we decided to choose Au, Ag, Cu, Pd, Ga, Sn, Co, Ni and Fe for our calculations. Notice that this choice also creates a diverse set of metals including base, noble and low-melting point metals that allows us to examine how metal characteristics impact the energetics and plausibility of studied reactions.

Accordingly, we emphasize that while one practical motivation of the calculations here is the parametrization of future kinetic models, we set the scope for this work to the analysis of the energetics of reactants, product and transition states on different metals, metal-based energetic trends, and the general plausibility of proposed reactions. This is to take advantage of the fact DFT calculations have the potential to provide clarity to experiments by decoupling and examining reaction events in significantly more controlled fashion than experiments can. To enrich the discussion around reaction energetics and plausibility, we complemented our DFT calculations with NH_3 synthesis experiments in a DBD reactor and optical emission spectroscopy (OES) characterization of the corresponding plasmas. Finally, we accompany the reaction energetics analysis with the exploration of the potential for energetic data to explain and/or predict trends on experimental data, including measured trends on turnover frequencies (TOFs) across different metals. As an example of the latter, we examined correlations between reaction energies of studied reactions and TOFs for experiments herein performed as well for others reported in the literature.

■ METHODS

Experiments.

Reactor Setup. The catalytic activity for different metal electrodes was assessed in an in-house DBD reactor (**Fig. 1**).

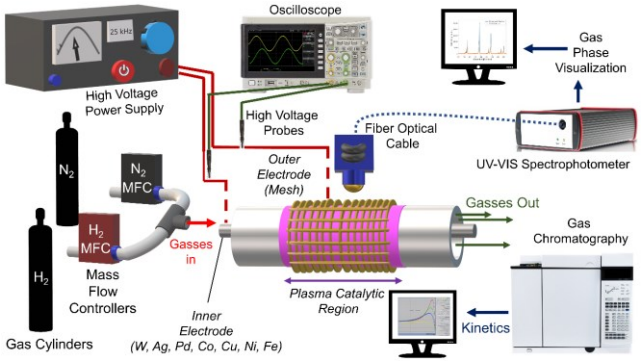

Fig. 1. General schematic and details of the Plasma Catalytic Dielectric Barrier Discharge (DBD) reactor employed

The reaction setup comprises (1) the plasma reactor core, (2) the optical emission spectroscopy system, (3) the oscilloscope, and (4) the gas chromatograph (GC). For the catalytic tests, N_2 and H_2 cylinders were connected to the reactor using mass flow controllers. The reactions were carried out at 25 sccm of total flow rate with equimolar feed ratio of nitrogen to hydrogen (1:1) (N_2:H_2), at a plasma power of 15 Watts (unless noted otherwise). The average bulk temperature of the reactor was 125°C (± 2.8°C) with a fan continuously running during reaction time. The applied voltage was measured to be 12 ± 0.5 $kV_{pk\text{-}pk}$ with frequency of 25 ± 0.5 kHz. To determine the ammonia synthesis rate, the exhaust gas was sent to the gas chromatograph calibrated for ammonia synthesis. The quantification was performed using an Agilent 7820A GC equipped with a HP-PLOTU column (30 m × 0.320 mm × 10 µm) and hydrogen as carrier gas. All electrodes were pre-treated with hydrogen plasma for 10 minutes at a constant power of 5 Watts before conducting the reaction. This had the main purpose of cleaning the metal surface from any native oxide content.

***Metal electrodes*.** All the metal electrodes employed in this study had 2.0 mm diameter and 152 mm length. Alfa-Aesar, 99.995% metal basis wires were employed for Co, Ni, Ag, Cu, and Fe electrodes, wire supplied by Surepure Chemetals Inc. for Pd electrodes, and wire from Midwest Tungsten Service for the W electrode. The high voltage power supply was connected to the reactor using a litz wire and alligator clips. The inner electrodes were placed at the center of the quartz tube with an i.d. of 4 mm and an o.d. of 6.35 mm. The connectors were made of polypropylene to avoid an arc formation. The outer electrode was made of tinned copper mesh acting as the ground electrode.

Electrical Measurements. The electrical characterization was carried out by measuring the applied voltage to the reactor by employing a high voltage probe (Tektronix P6015A). The charge was calculated using the voltage measurement across a capacitor. The two probes are connected to an oscilloscope (Tektronix TDS2014C). The capacitor was connected to the reactor in series with the ground electrode.

***Optical Emission Spectroscopy*.** The light emitted from the discharge was led through an optical system, and the emission spectra of the glow region were measured at the center of the tube. The measurements were recorded using a dual channel UV−vis−NIR spectrophotometer (Avantes Inc., USB2000 Series) in a scope mode. Spectral range from 185 to 1100 nm, using a line grating of 600 lines/mm and a resolution of 0.4 nm. A bifurcated fiber optic cable of 400 μm was employed. The spectral scans were conducted five times for each catalytic cycle with integration time of 3 seconds and scan/average of 100.

DFT calculations. Plane-wave density functional theory (PW-DFT) calculations were performed using the VASP.5.4.1 ab-initio code.[37–39] Calculations used the GGA Purdue-Burke-Ernzerhof (PBE) functional[40] to model the electron exchange and correlation, along with the D2 corrections by Grimme[41–43] to explicitly introduce dispersion interactions. An energy cutoff of 400 eV was used to define the basis set of Block waves to construct the solutions to the Kohn-Sham equations. All simulations used spin polarization. Smearing[44] at the Fermi level was used to accelerate energy convergence with respect to number of k-points, using the Methfessel-Paxton method of first order with a smearing parameter of 0.03 to keep T*S under 1 x 10^{-3} eV. Electronic and atomic configurations were considered converged when energy and forces fell below at least 10^{-5} eV and 10^{-2} eV/Å, respectively (10^{-3} eV/Å was used for configurations used as input for transition state finding methods).

The bulk unit cells of all metals were optimized, and the slabs for our calculations were cleaved from these unit cells using the Crystal Builder module of Materials Studio.[45] Bulk unit cells were optimized using 12 x 12 x 12 Gamma-centered k-point meshes. Lattice constants were within the expected accuracy for PBE (~2 %). The cleaved slabs were cut exposing the most stable facet of the metal. The slab for Ga was taken from our previous work.[20] The most stable facet for Sn was determined here based on surface energy calculations (see **Table S1**) and were at least 3-layered with at least 1 layer frozen, leaving at least 15 Å vacuum space between slabs in the direction perpendicular to the surface. A 4 x 4 x 1 k-point mesh was used for slab calculations, as further increasing the mesh density was found to not significantly alter adsorption energies. Calculations on isolated N_xH_y species were done at the gamma-point on a 20 Å x 20 Å x 20 Å orthogonal cell.

Vibrational frequencies were obtained using the finite-displacement method systematically displacing atoms 0.01 Å in all directions. Generally, vibrations of surface species were decoupled from the vibration of the heavier metal atoms by not performing displacements on them. Transition states were generally found using the climbing-image nudged elastic band (CI-NEB) method[46], with the transition state verified to have only one imaginary frequency. Typically, seven images were used to construct the band, which was optimized until forces fell below 5 x10^{-2} eV/Å. In a few cases, the highest image from the band was found not to have only one imaginary frequency, in which case the transition state was "refined" by using the dimer method[47] with the highest band image as input. For the dimer method the electronic and geometric configuration were considered converged when the energy and forces fell below 10^{-8} eV and 10^{-3} eV/Å, respectively.

Sorption and reaction energetics. Adsorption energies (ΔE_{ads}) were calculated as:

$$\Delta E_{ads} = E_{slab+N_xH_y} - E_{slab} - E_{N_xH_y} \qquad (1)$$

where $E_{slab+NxHy}$ is the energy of the slab with the adsorbed N_xH_y species, E_{slab} is the energy of the slab, and E_{NxHy} is the energy of the isolated N_xH_y species. For cases where we estimated the activation energy directly from CI-NEB calculations, the reaction energies were calculated as:

$$\Delta E_{rxn} = E_{slab+P} - E_{slab+R} \qquad (2)$$

where E_{slab+P} and E_{slab+R} are the energies of the slab with the products and reactants, respectively. Activation energies (E_a) were calculated as:

$$E_a = E_{TS} - E_R \qquad (3)$$

where E_{TS} is the energy of the transition state. For cases, where Bronsted-Evans-Polanyi (BEP) relationships were used to estimate activation energies, the needed input reaction energies (ΔE_{rxn}) to get E_a were calculated as:

$$\Delta E_{rxn} = E_{slab+P} + E_{slab} - E_{slab+R1} - E_{slab+R2} \qquad (4)$$

for LH reactions, where E_{slab+P}, $E_{slab+R1}$, and $E_{slab+R2}$ are the energy of the slab with the adsorbed product, reactant 1 and reactant 2, respectively, and as:

$$\Delta E_{rxn} = E_{slab+P} - E_{slab+R1} - E_{R2} \qquad (5)$$

for ER reactions, where E_{R2} is the energy of the isolated reactant 2. The BEP relationships used here were derived either by Norskov and coworkers[48] or by us from transition state data herein generated. More specifically, for a given reaction directly examined here with transition state finding methods, we found the transition state at least for three metals (chosen as to spread out the values of ΔE_{rxn}), and with the obtained values of E_a and ΔE_{rxn} we derived the corresponding BEP relationships to cost-effectively estimate E_a on the remaining metals. Note that the use of scaling relationships is necessary due to the large number of metal/reaction combinations relevant to plasma-assisted ammonia synthesis.

All the presented energetics was corrected with the zero-point energy (ZPE), which was calculated for every relevant configuration as:

$$ZPE = \sum_{i=1}^{n} h\nu_i/2 \quad (6)$$

where h is the Plank constant, ν_i is the frequency of vibrational mode i, and n is the number of vibrational modes.

■ RESULTS AND DISCUSSION

Optical emission spectroscopy of the plasma phase. To contextualize discussions on energetics and plausibility of reactions and experimental trends in following sections, we used OES to examine the plasma phase in our DBD reaction experiments. While recognizing that higher resolution OES could be obtained with more sophisticated equipment, we emphasize that our goal in this section is not to quantify species but rather to assess *i)* the plausibility of potentially key species existing in the plasma, *ii)* abundance trends among these key plausible plasma species, and *iii)* whether there are dramatic differences in plasma composition across different metals. We start then by presenting in **Fig. 2** the OESs collected during reactions experiments in Fe and Ag, as we find the OESs for these two metals to make the most drastically different pair between studied metals. Fe-Ag turns out to be the pair with the most different nitrophilicity (see **Section 3.2**). Emissions at different wavelengths is suggestive of the presence of different plasma species. For instance, emission around 656 nm (**Fig. 2b**) corresponds to H_α emission (due to electron *decay* in an electronically excited H atom), being indicative of H_2 dissociation in the plasma and thus suggestive of the presence of H• radicals in the plasma phase.[28] This is an emission also detected in our earlier (sub-atmospheric pressure) RF experiments[20], suggesting that H• radicals could play an important mechanistic role at a wide range of reactor pressures.

In **Fig. 2a**, the emission corresponding to electron decay within N_2 ($[C^3\prod_u \rightarrow B^3\prod_g]$ transition) is shown, being orders of magnitude higher intensity in the OES than H_α. This is consistent with (expected) dramatically higher abundance of (neutral) non-dissociated N_2 species than H•. Unclear from **Fig. 2a**, however, is the emission normally ascribed to NH[$A^3\prod - X^3\prod$] transition, which shows up at 336 nm.[28] Thus, we conducted time-lapsed experiments in Ag (**Fig. 2d**) and Fe (**Fig. 2e**), which show how the 336 nm feature becomes more apparent with time, ultimately being suggestive of the presence of NH species in the plasma (and hence NH• radicals). Plausibly, NH species originate from NH_3 product dissociation. And indeed, as shown later in this work**,** we find OES intensity at 336 nm to correlate well with NH_3 TOFs. However, due to the influence of the tail of the $N_2[C^3\prod_u \rightarrow B^3\prod_g]$ transition one should be careful not to interpret the intensity at 336 nm (which is several orders of magnitude higher than for H_α) as indicative of NH• radicals being orders of magnitude more abundant than H• radicals.

Fig. S5c, on the other hand, shows that a distinctive 746 nm emission (N[3p →3s] transition), which would be correlated to atomic nitrogen,[28] was not detectable at typical conditions for our reaction experiments. This is consistent with N_2 dissociation being significantly more difficult to form than H_2 dissociation, thus harder to detect. However, **Fig. 2c** shows the distinctive emission at 746 nm in the OES when only N_2 was fed to the reactor, indicating that at the plasma power used in our reaction experiments (15 W), N_2 can dissociate (and hence form N• radicals). Also, notice that with a small increase in plasma power (to 20 W), the 746 nm emission feature can also be distinguished when co-feeding N_2 and H_2 (**Fig. 2f**). Accordingly, the observations discussed

.

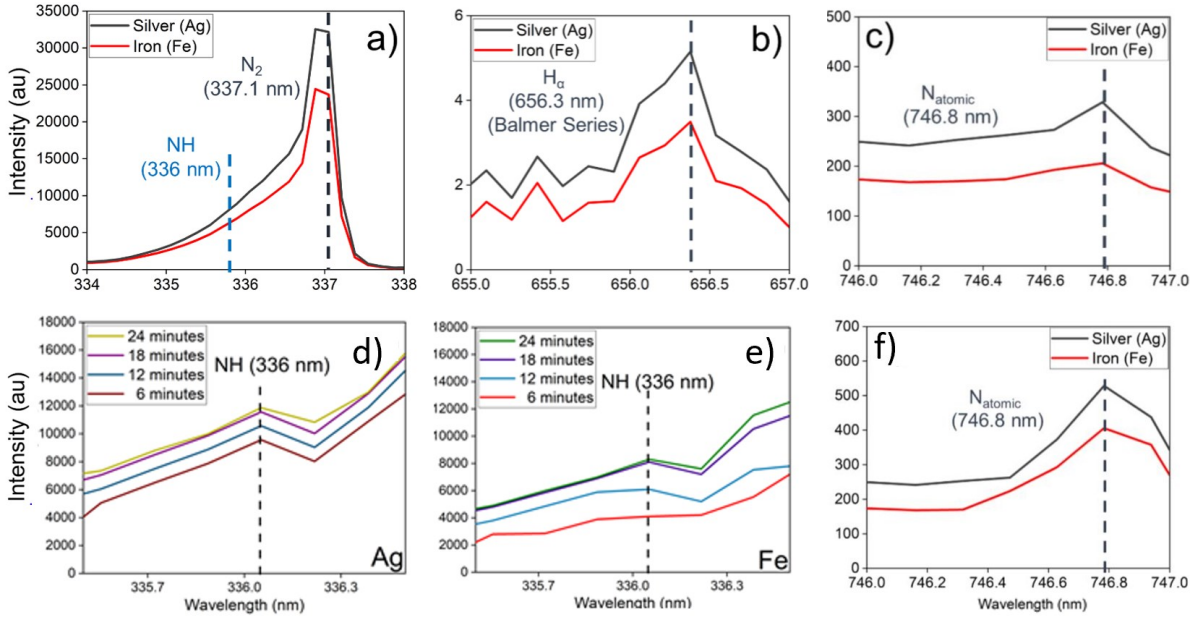

Figure 2. Optical emission spectra (OES) characterization of the plasma phase in the presence of Ag and Fe in a DBD reactor. Emissions at different wavelengths can be used to infer the presence of different species. (a) Emissions at 337 nm and 336 nm, which can be used to infer the presence of N_2 and NH species, respectively (b) H_α emission, which can be used to infer the presence of atomic hydrogen. (c, f) emission at 746 nm, which can be used to infer the presence of atomic nitrogen. (d,e) Time-lapsed OES collection confirming the 336 nm emission feature associated with NH species. The reaction temperature was 125 C in (a-f), N_2:H_2 ratio was one in (a, b, d-f), and infinite in (c). Plasma power was 15 W in (a-e) and 20 W in (f).

Table 1. Relative emission intensities (REI) in the plasma OES calculated for experiments with different metals catalytically tested in a DBD reactor with respect to experiments with the W electrode. The species correlated with the emission wavelength are shown in parentheses. Each OES was collected five times, hence standard deviation (σ) is also shown.

	Ag		Cu		Pd		Co		Ni		Fe	
Emission	REI	σ	REI	σ	REI	σ	REI	σ	REI	σ	REI	σ
336 nm (NH)	0.66	0.09	0.56	0.01	0.61	0.02	0.56	0.04	0.50	0.03	0.43	0.03
337 nm (N_2)	0.64	0.08	0.62	0.02	0.57	0.03	0.52	0.04	0.47	0.03	0.48	0.02
391 nm (N_2+)	1.40	0.15	1.20	0.02	1.11	0.03	1.12	0.13	1.08	0.06	1.16	0.04
656 nm (H)	5.15	0.46	4.71	0.66	2.94	0.22	4.40	0.19	3.72	0.40	3.49	0.22

at to this point are consistent with the following theses: *i)* neutral non-dissociated N_2 species are significantly more abundant than plasma radicals, *ii)* H• radicals are more abundant than N• radicals, and *iii)* NH radicals exist in the plasma, plausibly due to product NH_3 dissociation.

Now we proceed to assess to whether the plasma phase changes dramatically with metal. To this end, we compare the relative emission intensities (REI) for reaction experiments with different metals (**Fig. S6**) at the wavelengths described in the previous paragraphs. Given the impossibility of using metal-free DBD experiments as reference, **Table 1** shows the emission intensities relative to the corresponding emission intensity for experiments with a W electrode. The idea is that dramatic differences in the REIs at key features of the spectra across the tested metals would indicate dramatic differences in the plasma compositions, which would in turn be indicative of the ability of the catalyst to dramatically affect the exact composition of the plasma.

To consider statistics for this comparison, for each metal, the OES was collected five times (at different days), resulting in the standard deviations, σ, presented in **Table 1**. Using the average REI and σ in **Table 1**, *t*-tests were done to assess whether differences between different metal pairs were statistically significant. Out of 60 REI comparison between metal pairs, 74% were statistically significant. However, the largest REI difference between any two metals does not exceed 40% for emissions at 336 nm and 391 nm (those associated with N_2 and N_2+), 47% for 656 nm emissions (H_α emissions), and 53% for 336 nm emissions associated (those associated with NH). Based on this, we ascertain that while differences in the plasma phase between metal may be statistically significant, the effect of metal identity on the plasma composition is weak, in agreement with postulates by Go and coworkers.[49]

Interestingly, despite the weakness of the effect, the REIs in **Table 1** present moderate to strong correlations with the adsorption energy for the associated species as calculated from DFT in later sections (**Fig. S7**). For instance, H_α REI correlates with H• adsorption energy ($R^2 = 0.64$), which is a significant difference with measurements in our earlier experiments in a RF reactor, for which H_α emission intensity presented a distinctive volcano-type relationship with this adsorption energy. Meanwhile, emissions at 336 nm (associates with NH) correlates rather strongly with NH• adsorption energy (R^2=0.87). Regardless, the weak metal effect on the plasma phase indicates that differences in how plasma species interact with the catalysts surface and how subsequent reactions proceed is the primary reason for difference in NH_3 formation rates across different metals. Now we proceed to examine these factors with DFT.

Adsorption energies. As we will see through DFT calculations in a later section, the presence of H• and N• radicals in the plasma phase is likely the crucial factor facilitating the formation of N_YH_X species experimentally detected by Chen and coworkers[30] and Koel and coworkers.[31] Thus, in this section, we discuss all ZPE-corrected adsorption energies (and adsorption site information) for all N_YH_X species on the most stable (most closely packed) surface for each metal—with the exact values presented in **Table S2**. Due to their lower surface energy, the studied surfaces would be the most abundantly exposed surface on the corresponding metal catalyst. Although we find the ZPE correction for the adsorption energy of a given species to be similar across different metals, without this correction, adsorption strength could be overestimated as much as 0.24 eV (**Table S3**). As previous works suggest an inverse correlation between nitride formation tendency and catalyst performance under plasma conditions, here we discuss the nitrophilicity of nine metals as measured by the N* adsorption energy. Per this metric, nitrophilicity follows the order Ag < Au < Cu < Sn < Ga < Pd < Co < Ni < Fe, making all studied metals less nitrophilic than Fe—the standard catalyst for thermal ammonia synthesis.

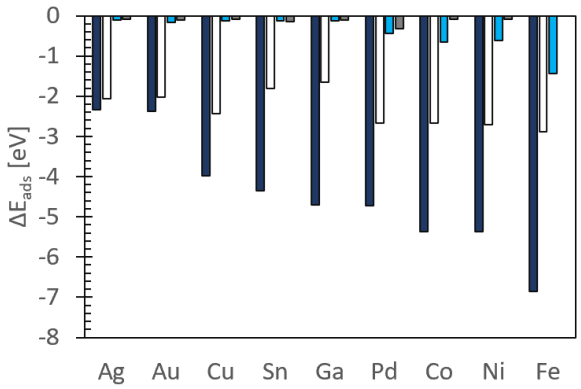

Figure 3. Adsorption energies for N*, H*, N_2*, NH_2* on the studied metal surfaces. N* (dark blue), H* (white), N_2* (light blue), H_2* (gray).

N_2, H_2, N and H adsorption. Adsorption energies for these species are presented in **Fig. 3**, with the corresponding adsorption configuration available on **Fig. S8.** N* is pertinent to the adsorption of N• radicals. N* is most stable on hollow sites on most metals, except on Fe where it is most stable on long-bridge sites. The N* adsorption energy ranges between -2.34 eV in Ag to -6.86 eV in Fe. N_2* is pertinent to the non-dissociative adsorption of $N_{2(g)}$, which remains as a majority species in the

plasma (**Fig. 2a**). However, the adsorption of N_2* is much weaker than N*, ranging between -0.11 eV in Ag and -1.44 eV in Fe. As the nitrophilicity of the metal increases, the adsorption of $N_{2(g)}$ switches from physisorption to chemisorption. The switch point occurs between Ga and Pd, where the adsorption energy jumps from -0.13 eV in Ga to -0.44 eV in Pd, and the adsorption configuration changes from N_2 hovering on Ga (and less nitrophilic metals) to N_2 directly binding a surface site in Pd (and more nitrophilic metals). Intriguingly, this switch occurs despite almost identical N* adsorption energies for Pd and Ga. The N_2 binding occurs vertically on a top site for Pd, Co, Ni, and switches to horizontally on Fe (the most nitrophilic metal).

H* is pertinent to the adsorption of H• radicals, which are presumably more abundant than N• due to the H-H bond being weaker relative to N≡N (4.5 eV vs. 9.6 eV), in consistency with the easier detection of H_α emissions than those of associated with atomic nitrogen (**Fig. 2**). H* is most stable on hollow sites on all studied metals, including the less conventional hollow sites of Ga and Sn (**Fig. S2-S3**). The H* adsorption energy ranges between -1.80 eV for Sn and -2.88 eV for Fe. In all metals, the adsorption of H* is weaker than for N*, but stronger than for N_2*. H_2* is pertinent to non-dissociative adsorption of $H_{2(g)}$, which is the weakest among all species herein studied. $H_{2(g)}$ was physisorbed on all metals except Pd and Fe, adopting a vertically hovering position with adsorption energies in the -0.08 eV to -0.15 eV range. On Pd, H_2* chemisorbs adopting a horizontally bound position on a top site, with an adsorption energy of -0.32 eV. On Fe, we did not find H_2* to be stable, finding it to spontaneously dissociate to 2H* in all our geometry optimization attempts, which is consistent with Fe presenting a negligible barrier for $H_{2(g)}$ dissociative adsorption.

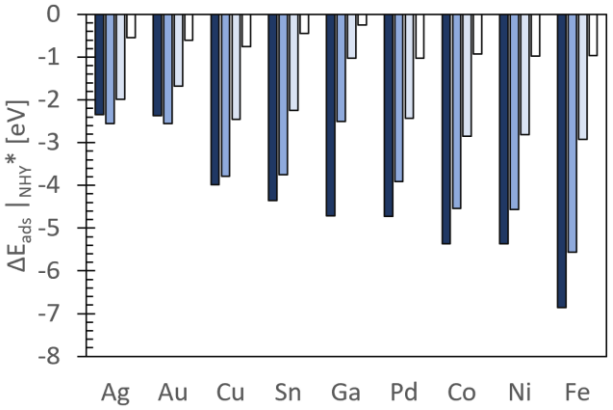

Figure 4. Adsorption energies for NH_Y* species on the studied metal surfaces. As hydrogenation level increases (as Y changes from 0 to 3) bar color changes from dark blue to white.

N_2* and H_2* can also be the basis to discuss adsorption of vibrationally excited N_2 and H_2, where changes in $h\nu$ as these species adsorb can be inferred from ΔZPE data in **Table S3**. Based on the change of $h\nu$ between the isolated and adsorbed N_2 ($\Delta h\nu|_{N2}$), N_2* adsorption energies are directly descriptive of the adsorption of $N_2(v)$ on Ga and less nitrophilic metals. However, for Pd and more nitrophilic metals, $\Delta h\nu|_{N2}$ ranges between 0.04 eV and 0.12 eV, making the adsorption of $N_2(v)$ in these metals less favorable than for N_2. The change of $h\nu$ between isolated and adsorbed H_2 ($\Delta h\nu|_{H2}$) is -0.02 eV on all metals except Pd, making adsorption of $H_2(v)$ slightly more favorable than for H_2. The opposite is true for $H_2(v)$ on Pd, since $\Delta h\nu|_{H2}$ is 0.16 eV in this case.

There is a strong correlation between N* and N_2* adsorption energies when N_2* chemisorbs (R^2 = 0.98, **Fig. S9a**), but not when N_2 physisorbs (R^2=0.03, **Fig. S9b**). This is unsurprising as chemisorption of both N_2* and N* is expected to follow the trends from the d-band model[50] (i.e., higher d-band center equals stronger adsorption), whereas physisorption of N_2* is not expected to do so. Consistent with this idea, there is no correlation between N* and H_2* adsorption energies due to the physisorption character of the latter (R^2= 0.03, **Fig. S10**). But there is a weak correlation between N* and H* adsorption energies (R^2 = 0.36, **Fig. S11a**), which becomes strong when Ga and Sn—two post-transition metals that do not follow the d-band model—are obviated (R^2 = 0.96, **Fig. S11b**). In other words, Ga and Sn adsorb H* weaklier than expected from their binding strength to N*.

NH_Y adsorption. Adsorption energies for these species is presented in **Fig. 4**, with the corresponding adsorption configurations available on **Fig. S12**. NH_Y species form on the catalyst surface under the accepted HB mechanism but could also form in the plasma (albeit most plausibly from NH_3 decomposition) and adsorb on the metal surface. For instance, the presence of NH species was suggested by emissions at 336 nm in our collected OESs (**Fig. 2**). NH* adsorption energy ranges from -2.55 eV in Au to -5.56 eV in Fe, with NH* preferably adsorbing on hollow sites on all metals, except on Fe where it preferably adsorbs on long-bridge sites. More hydrogenated NH_Y species tend to adsorb weaklier, with the exception being NH* in Ag, on which the latter adsorbs weaklier than N*. NH_2* adsorption energy ranges

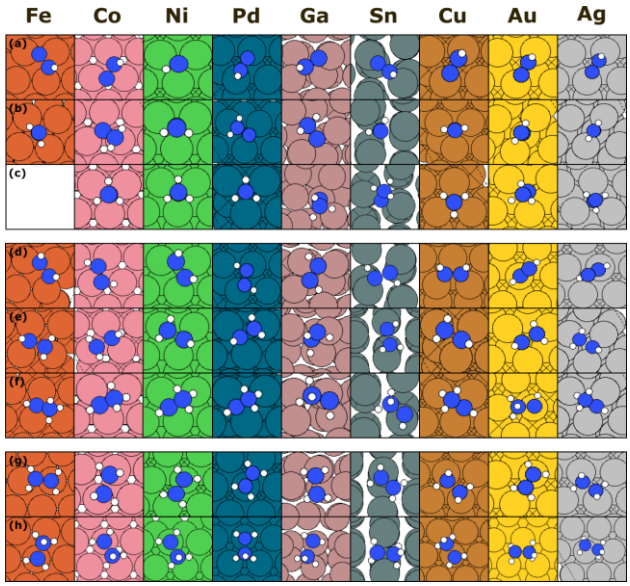

Figure 5. Top-view of most stable adsorption configurations for N_2H_Y species on studied metal surfaces. N-NH_Y species on top row ((a) Y = 1, (b) Y = 2, (c) Y = 3), HN-NH_Y species on middle row ((c) Y = 1, (d) Y = 2, (e) Y = 3), H_2N-NH_Y species on bottom row (((f) Y = 2, (g) Y = 3).

from -1.02 eV in Ga and -2.92 eV in Fe, with NH_2* adsorbing on bridge sites on all metals. NH_3* adsorption energy ranges between -0.25 eV in Ga to -0.97 eV in Ni, with NH_3 always adsorbing on top sites. Generally, adsorption weakening with NH_Y hydrogenation is more pronounced as the metal nitrophilicity increases (**Fig. 4**). The correlation between NH_Y* and N* adsorption energy weakens as Y increases (from R^2 = 0.74 to R^2 = 0.24), but it is also stronger when Ga and Sn are ignored (with R^2 ranging from 0.99 to 0.78) (**Fig. S13**). Interestingly,

when considering all metals, the adsorption energy of the more hydrogenated species correlates better with H* adsorption energy. For instance, NH_3* and H* adsorption energies correlate with $R^2 = 0.95$ (**Fig. S14**). Before discussing N_2H_Y species, note that, where possible to compare, our calculated binding energies (and stable adsorption sites) for N*, H*, NH*, NH_2* and NH_3* agree relatively well with calculations by Norskov and coworkers[51], as well as Mavrikakis and coworkers[52–55] despite use of different functionals by these authors (RPBE and PW91, respectively). Moreover, the agreement improves when considering *differences* in binding between metals.

N_2H_Y adsorption. An overview of adsorption configurations for these species is shown in **Fig. 5**. N_2H_Y species are seldom considered in the HB mechanism[56], but often considered for electrochemical ammonia synthesis[12] where the associative mechanism is thought to come into play[57]. Given the experimental detection of N_2H_Y species,[30] this mechanism may also be relevant to plasma-assisted ammonia. The associative mechanism starts with the formation of N-NH*, which preferentially adsorbs horizontally in all studied metals except Ni where it adsorbs vertically on a hollow site. On Au, Ag, Cu, Sn, Ga, and Pd, both N atoms adsorb on hybrid bridge-top positions, whereas on Co, and Fe, both atoms are on bridge positions. N-NH* adsorption energy ranges from -0.38 in Au to -3.06 eV in Fe. N-NH* and N* adsorption energies correlate well for all metals (R^2= 0.80) but correlate better when Ga and Sn are ignored (R^2= 0.97) (**Fig. S15**). This is consistent with the tendency by Ga and Sn to adsorb other species weaklier than expected from their binding strength to N*.

N-NH* can be hydrogenated through the NH "bead," which leads to N-NH_2* and N-NH_3* formation, with the adsorption energy increasing as hydrogenation increases (**Fig. 6a**), presumably due to the weakening of the N-N bond, which makes the hydrogen-free N increasingly interact more like N*. In fact, in Fe—the most nitrophilic metal—this is so that N-NH_3 spontaneously breaks into N* and $NH_{3(g)}$. Both N-NH_2* and N-NH_3* tend to bind vertically (N-NH_2* tilts on Ga, Pd and Co). In N-NH_2* the hydrogen-free N tends to bind on bridge sites (binding on hollow sites only on Cu, Sn, Ni), whereas in N-NH_3* the hydrogen-free-N tends to bind on hollow sites (binding on bridge sites only on Sn) (**Fig. 5**). Despite the adsorption of N-NH_Y becoming more N*-like as hydrogenation increases, the adsorption energies of N-NH_2* and N-NH_3* correlate less with that of N* ($R^2 \sim 0.7$) than N_2H* does (**Fig. S15**). Interestingly, when Ga and Sn metals were ignored, the adsorption energy of N-NH_3 correlates better with N* adsorption energy ($R^2 \sim 0.99$) because the N-N bond between the hydrogen-free N and NH_3 is weak, and the hydrogen-free N is very similar with the simple N*.

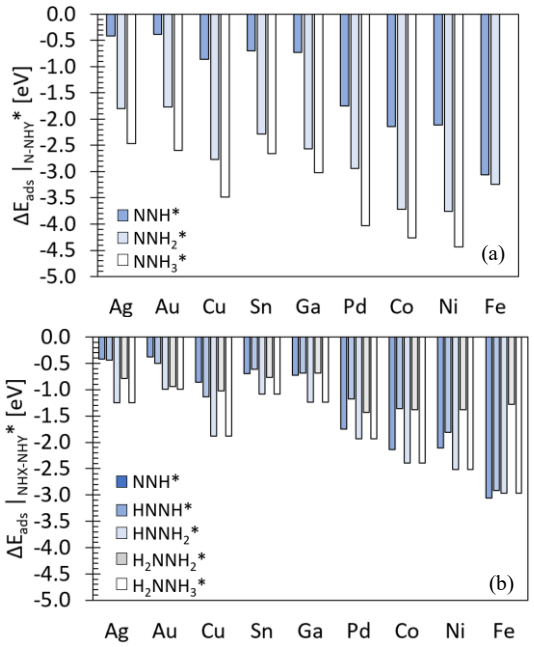

Figure 6. Adsorption energies for species emerging during sequential hydrogenation of NH bead of NNH (a) and during staggered hydrogenation of NNH (b). For each metal, as bar decolorize (from left to right), hydrogenation increases.

N-NH* can also be hydrogenated in staggered fashion to form HN-NH*, HN-NH_2*, H_2N-NH_2* and H_2N-NH_3*. Among these, HN-NH* and H_2N-NH_2* are molecular species (diazene and hydrazine, respectively) that tend to adsorb weaklier than HN-NH_2* and H_2N-NH_3*. Therefore, adsorption trends with hydrogenation and metal nitrophilicity, while rationalizable, are not simple (**Fig. 6b**). HN-NH* shifts from likely to desorb in Ag (ΔE_{ads}=-0.44) to unlikely to desorb in Fe (ΔE_{ads} = -3.12 eV). Except on Cu, Ni, and Fe, HN-NH* was most stable on its *trans* configuration. H_2N-NH_2* adsorption energies range from -0.68 eV on Ga to -1.43 eV on Pd. Similar to NH_3*, H_2N-NH_2* adsorption energies correlate better with that of H* (R^2 = 0.88, **Fig. S17**) than with that of N* (R^2 = 0.35, **Fig. S16**).

H and N dissolution. "Adsorption" energies at the most favorable dissolution subsurface sites are presented in **Table S2**, along with indication of the type of site. Typical dissolution reaction pathways and all transition states are presented in **Fig. S18**. Again, these calculations were motivated by the hydrogen-sink effect postulated to aid catalyst performance by removing H* from the surface, hence hindering recombination to H_2(g) and boosting H* availability for reaction pathways that lead to NH_3.[20] We denoted subsurface sites as "◇" and dissolved H as H◇, which was generally found to be more stable on octahedral subsurface sites, except on Pd (tetrahedral site), Ga (distorted tetrahedral site) and Sn (distorted hexagonal prism). Pd, as expected from its use in hydrogen membranes[58], binds H◇ more strongly (-2.38 eV) than other metals studied here, with a binding almost as strong as the corresponding H* adsorption. Metals such as Cu, Co, Ni and Fe also bind H◇ strongly (between -1.84 eV and -2.10 eV) but noticeable less so than the corresponding H*. Accordingly, we generally observed positive reaction energies for:

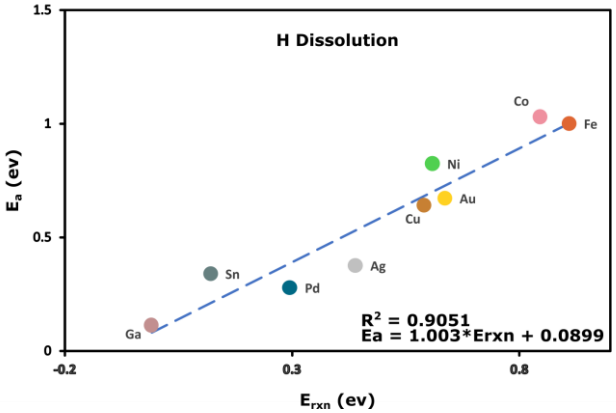

Figure 7. BEP relationship between activation and reaction energies for H dissolution reaction (*r1*). R^2 = 0.90.

$$H^* + \diamond \rightarrow * + H\diamond \quad (r1)$$

which range from -0.01 eV for Ga to 0.91 eV for Fe, and which present only moderate (inverse) correlation with H* adsorption energies ($R^2 = 0.54$, **Fig S19**). However, a strong correlation was found between the reaction and activation energies for the dissolution reaction *r1* ($R^2 = 0.90$, **Fig. 7**), even though the activation energy for Fe dissolution was taken from ref. [59,60]. Metals seem to cluster into three groups based on to what extent hydrogen dissolution is facilitated in them: Ga, Sn, Pd and Ag ($E_a < 0.4$ eV), Cu, Ni, Au (0.6 eV $< E_a <$ 0.9 eV) Co and Fe ($E_a >$ 1.0 eV).

Nitride formation is another process that has been suggested to impact ammonia formation.[20] Nitride formation likely requires nitrogen dissolution to the bulk, motivating us to inspect the dissolution reaction *r2*:

$$N^* + \diamond \rightarrow * + N\diamond \quad (r2)$$

The reaction energy for *r2* ranges from -0.15 eV in Ga to 1.61 in Fe, with only a moderate (inverse) correlation with N* adsorption energies ($R^2 = 0.53$, **Fig S20**). Similar to *r1*, the inverse correlation arises because the stronger the surface adsorption is, the less likely the subsurface binding is to match it. Given, the strong correlation between reaction and activation energies ($R^2 = 0.96$, **Fig. S21**), the less nitrophilic metals tend to have lower dissolution barriers. The exception is Ga and Sn, whose low activation energy for *r2* (and *r1*) is likely due to their "open" structures which allows for metal atom mobility as N (and also H) goes from the surface to the subsurface. For instance, an inspection to **Fig. S18** show the significant rearrangement of metal atoms in the dissolution transition states in Sn.

ER reactions. Given the experimentally detected presence of radicals in N_2/H_2 plasmas, one of the major differences between plasma-assisted and thermocatalytic ammonia synthesis is that in the former ER reactions where plasma radicals react with surface-bound species become plausible.

ER activation barriers. In our previous work[20], we assumed a scaling relationship proposed by Bird et al.[61] to estimate barriers for ER reactions involving molecular species to hold for ER reactions involving radicals. On the other hand, Bogaerts and coworkers have recently assumed energy barriers for ER reactions involving radicals to be zero.[62] Thus, to examine the typical barrier for ER reactions, we chose to directly study the reaction coordinates for reactions *r3* to *r8* using CI-NEB calculations on at least three metals each:

$$H\bullet + N^* \rightarrow NH^* \quad (r3)$$
$$N\bullet + H^* \rightarrow NH^* \quad (r4)$$
$$H\bullet + N_2^* \rightarrow NNH^* \quad (r5)$$
$$N\bullet + NH^* \rightarrow NNH \quad (r6)$$
$$H\bullet + NH^* \rightarrow NH_2^* \quad (r7)$$
$$H\bullet + NH_2^* \rightarrow NH_3^* \quad (r8)$$

The above reactions represent a diversity of ER reaction scenarios. For instance, whereas for *r3* we expected H• to be able to land directly on N to form NH* without a barrier, for *r4* we were uncertain whether NH having to flip upon N• landing on H* would manifest on a barrier. *r5* represents a scenario where a radical collides with a weakly bound molecule, *r6* where a radical has to "scoop up" a strongly bound species, *r7* and *r8* where upon collision with the radical the bound species has to migrate to a different adsorption site. To set up the reactant state for each of these calculations we *i)* took the optimal configuration for the product from **Section 3.2** and displaced either the H or N atom assumed to come from the radical vertically up to 3.0 Å from their position in the product and froze it at that location, *ii)* took the "leftover" surface-bound species (the reactant) and (as needed) moved to the nearest adsorption site known to be optimal for it from **Section 3.2**, *iii)* optimized the reactant state. Once this was done, we built intermediate configurations between reactant and product states using interpolation and ran CI-NEB calculations as described in **Section 2.2**.

A bird's eye view of energy vs. reaction coordinate plots is presented in **Fig. S22**. Our calculations were unable to reveal a barrier/transition state for any of the tested ER reactions on any of the tested metals. Representative reaction coordinates for *r3-r8* reactions on assorted metals are presented on **Fig. 8** to gain insights on how these reactions proceed. For *r3*, we observe the reaction to proceed as expected with an H• radical able to simply land on N* to form NH*. For *r4*, we observe that a close enough N• radical can abstract surface-bound H* to form an NH• radical slightly away from the surface, which then rotates as it falls back on the surface as NH*. For *r5*, we observe that a H• radical on collision course with the surface can attract a "hovering" N_2* to form NNH• slightly away from the surface, which then lands as NNH*. For *r6*, we observe that a N• radical close enough to a surface-bound NH* can abstract the H atom to form a NH• radical that rotates as it lands on the leftover N* to form NNH*. For *r7* (and *r8*), we observe that a H• radical on collision course with the surface can attract a nearby NH* (NH_2*), which starts to move from a hollow (bridge) site to a bridge (top) site to form NH_2* (NH_3*).

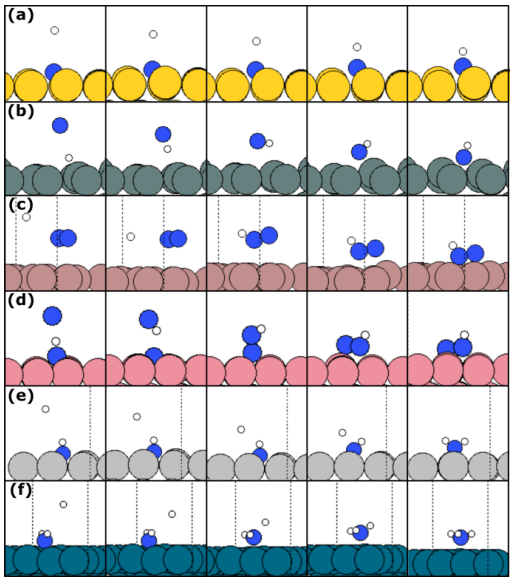

Figure 8. Reaction coordinates for ER reactions *r3 to r8*. (a) *r3* on Au, (b), *r4* on Sn (c) *r5* on Ga, (d) *r6* on Co, (e) *r7* on Ag, (f) *r8* on Pd.

Table 2. Estimated entropic barrier (TS_a) in eV at different temperatures and partial pressures for ER reactions involving the H• or N• radical. The assumption is that the radical loses one degree of freedom in a reactant-like transition state.

H• radical	N• radical

P [bar]	T = 398 K	T = 673 K	T = 398 K	T = 673 K
1 x 10^{-6}	0.32	0.56	0.36	0.64
1 x 10^{-5}	0.29	0.51	0.33	0.59
1 x 10^{-4}	0.26	0.47	0.31	0.55
1 x 10^{-3}	0.24	0.43	0.28	0.50
1 x 10^{-2}	0.21	0.38	0.26	0.46
1 x 10^{-1}	0.18	0.34	0.23	0.41
1	0.16	0.29	0.20	0.37

The above suggests that the assumption that ER reactions involving plasma radicals generally do not present energy (enthalpic) barriers is acceptable. Note, however, that ER reactions still must overcome entropic barriers as the inability of our CI-NEB calculations to reveal barriers does not preclude relevant transition states from existing. Rather, the implication is that the transition state elusiveness is due to excessive resemblance to the reactant state (as opposed to product state given the high exothermicity of the reaction). One interpretation of this picture is that the major change between the reactant and transition state for an ER reaction is *at least* the loss of one degree of freedom by the H• or N• radical (as a transition state always presents one less degree of freedom that reactants and products), with the entropy of activation S_a corresponding to the loss of one third of the entropy the radical possesses in the gas phase. For this assumption, as a reference for discussion, **Table 2** presents TS_a at 673 K and 398 K. These reaction temperatures correspond to our earlier RF experiments and our current DBD experiments, respectively. Per this calculation, ER reactions involving a H• radical present entropic barriers lower than 0.56 eV and 0.32 eV at 673 K and 398 K, respectively, assuming H• radical concentration is not lower than 10^{-6} bar.

Under a similar assumption for concentration, for ER reactions involving a N• radical, the entropic barriers are lower than 0.64 eV and 0.36 eV at 673 K and 398 K, respectively. Based on these entropic barriers, the fact that $G_a \sim -TS_a$, and the reasonable assumption that for surface reactions $E_a \sim G_a$ (**Fig. S25**), we will be using a 0.5 eV as a *rough* threshold when discussing favorability of ER reactions versus surface reactions. Although we focus on $TS_a \sim 0.5$ eV, with the data at hand, one can adjust upcoming analysis with a different threshold depending on the assumptions of how much entropy the radical loses at the transition state. For instance, one could use a threshold of $TS_a \sim 1.0$ eV instead if one assumes that the radical loses two thirds of its entropy.

ER reaction energies. Given the negligible energy (or enthalpic) barrier for ER reactions, and the independence of the (low) entropic barrier from metal identity, we focus now on the favorability of ER reaction based on reaction energies. Reaction energies for 20 ER reactions considered in this work are presented in **Table S4**. These reactions include *i)* recombination reactions where a N• (H•) radical collides with N* (H*) to make $N_{2(g)}$ ($H_{2(g)}$), *ii)* NH_Y-making reactions, which only lead to ammonia, *iii)* and H_XNNH_Y-making reactions, which lead to diazene, hydrazine, and ammonia. Nitrogen and hydrogen ER recombination are more favorable when the adsorption strength of N* and H*, respectively, is weaker. For instance, since Ag adsorbs N* weaklier than on Fe, nitrogen recombination is more favorable on Ag (**Fig. S23**). Across all metals, nitrogen recombination (*r9*, ΔE_{rxn} ranging from -7.89 eV in Ag to -3.37 eV in Fe):

$$N\bullet + N^* \rightarrow N_{2(g)} \text{ (r9)}$$

is significantly more favorable than hydrogen recombination (*r10*, ΔE_{rxn} ranging from -2.45 eV in Sn to -1.37 eV in Fe):

$$H\bullet + H^* \rightarrow H_{2(g)} \text{ (r10)}$$

Competing with *r9* and *r10* are *r3* and *r4*, which lead to NH*. Once NH* is formed, ER hydrogenation can only follow the sequence:

$$H\bullet + NH^* \rightarrow NH_2^* \text{ (r11)}$$
$$H\bullet + NH_2^* \rightarrow NH_3^* \text{ (r12)}$$

However, *r11* must compete with *r6* (which forms NNH*) and *r12* must compete with *r13* (which forms NNH_2*):

$$N\bullet + NH_2^* \rightarrow NNH_2^* \text{ (r13)}$$

r6 and *r13*, however, are more thermodynamically favored (i.e., more exothermic) than *r11* and *r12*, consistent with a trend where ER reactions involving N• radicals tend to be more favorable than those involving H• radicals (**Fig. S24**). Once NNH* or NNH_2* is formed, ER hydrogenation can follow different sequences "assembled" from the following reactions:

$$H\bullet + NNH^* \rightarrow NNH_2^* \text{ (r14)}$$
$$H\bullet + NNH^* \rightarrow HNNH^* \text{ (r15)}$$
$$H\bullet + NNH_2^* \rightarrow NNH_3^* \text{ (r16)}$$
$$H\bullet + NNH_2^* \rightarrow HNNH_2^* \text{ (r17)}$$
$$H\bullet + HNNH^* \rightarrow HNNH_2^* \text{ (r18)}$$
$$H\bullet + NNH_3^* \rightarrow HNNH_3^* \text{ (r19)}$$
$$H\bullet + HNNH_2^* \rightarrow HNNH_3^* \text{ (r20)}$$
$$H\bullet + HNNH_2^* \rightarrow H_2NNH_2^* \text{ (r21)}$$
$$H\bullet + HNNH_3^* \rightarrow H_2NNH_3^* \text{ (r22)}$$
$$H\bullet + H_2NNH_2^* \rightarrow H_2NNH_3^* \text{ (r23)}$$
$$H\bullet + H_2NNH_3^* \rightarrow 2NH_3^* \text{ (r24)}$$

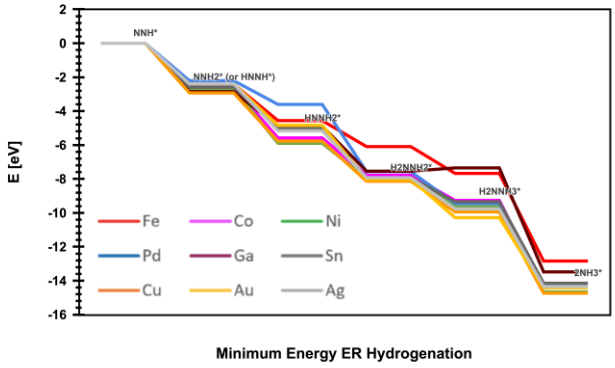

Figure 9. Minimum energy ER hydrogenation pathway for NNH* on studied metals. For the N_2H_2 intermediate, NNH_2* is most stable on Ni, Co, Pd, Ga, and Cu, whereas HNNH* is most stable on Fe, Sn, Au, and Ag.

If we assume that the most thermodynamically favored hydrogenation sequence is dominant, upon formation of

NNH* via *r6,* Fe, Sn, Au, and Ag would follow the hydrogenation sequence *r15* (HNNH*) → *r18* ($HNNH_2$*) → *r21* (H_2NNH_2*) → *r23* (H_2NNH_3*) → *r24* ($2NH_3$*), whereas Ni, Co, Pd, Ga, and Cu would follow the sequence *r14* (NNH_2*) → *r17* ($HNNH_2$*) → *r21* (H_2NNH_2*)) → *r23* (H_2NNH_2*) → *r24* ($2NH_3$*). On the other hand, upon formation of NNH_2* via *r13*, all metals would follow the hydrogenation sequence *r17* ($HNNH_2$*) → *r21* (H_2NNH_2*) → *r23* (H_2NNH_2*) → *r24* ($2NH_3$*). Notably, hydrazine (a species detected in some plasma-assisted ammonia synthesis experiments[19,63]) is an intermediate in all the above pathways.

Fig. 9. Illustrates the energetics of these minimum energy hydrogenation sequences for each metal starting from NNH*. The hydrogenation process is a continuously downhill process except on Ga, where H_2NNH_3 formation is an endothermic step. In the first hydrogenation step, NNH_2 is most stable in most studied metals, except on Fe, Sn, Au, and Ag where HNNH has lower energy. An important observation from **Fig. 9** is that the hydrogenation steps tend to become more favorable the less nitrophilic the metal is. However, as H_XNNH_Y hydrogenation increases, dissociation reactions become more likely (see below), in which case hydrogenation would continue individually on the produced NH_X and NH_Y fragments.

Dissociation reactions. Reaction and activation energies for 10 dissociation reactions are presented in **Table S6**. We start our discussion with reactions *r25* and *r26*, which in traditional HB ammonia synthesis are the sole source of N* and H* for subsequent NH_Y* formation:

$$N_2* + * \rightarrow 2N* \text{ (r25)}$$
$$H_2* + * \rightarrow 2H* \text{ (r26)}$$

Using scaling relationships[27], we estimate the barrier for *r25* to range from 1.64 eV on Fe to 6.77 eV on Ag. Again, assuming that entropic contributions for surface reactions are such that E_a and G_a (free energy of activation) are similar (a reasonable assumption for discussion purposes as shown in **Fig. S25**), then it is likely that above some critical radical concentration, N• radicals (even as a minority species) are the dominant source of N* even on Fe. Similarly, using scaling relationships[48], we estimate the energy barrier for *r26* to range from 0.85 eV to 1.27 eV on Ag, Au, Ga, and Sn. Thus, above a critical radical concentration, H• radicals are the likely dominant source of H* on these metals. On the other hand, the energy barrier for *r26* ranges from 0.08 eV to 0.36 eV on Co, Ni, Pd and Cu, which could make *r26* competitive as a source of H* (especially on Fe, Ni, Co). Incidentally, the barrier for *r26* on Fe is likely negligible in consistency with our observation of spontaneous dissociation when attempting to optimize H_2*.

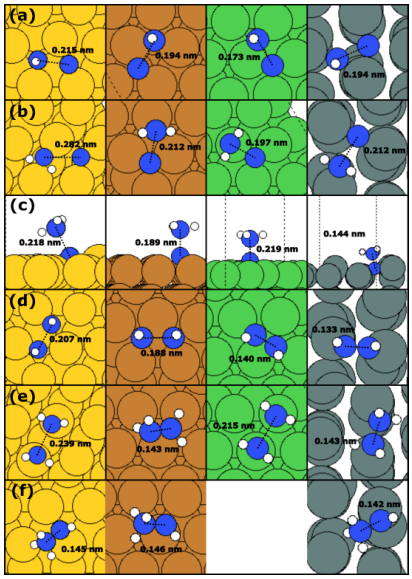

Figure 10. Transition states for dissociation reactions r27 (a), r28 (b), r29 (c), r30 (d), r33 (e) and r32 (f) on Au (yellow), Cu (orange), Ni (green) and tin (gray).

Regardless of the dominant source for N* and H*, in the plasma-assisted process, the reaction energetics discussed so far is supportive of the presence of radicals facilitating the formation of H_XNNH_Y species, which could dissociate according to:

$$NNH* + * \rightarrow N* + NH* \text{ (r27)}$$
$$NNH_2* + * \rightarrow N* + NH_2* \text{ (r28)}$$
$$NNH3* + * \rightarrow N* + NH_3* \text{ (r29)}$$
$$HNNH* + * \rightarrow 2NH* \text{ (r30)}$$
$$HNNH_2* + * \rightarrow NH* + NH_2* \text{ (r31)}$$
$$HNNH_3* + * \rightarrow NH* + NH_3* \text{ (r32)}$$
$$H_2NNH_2* + * \rightarrow 2NH_2* \text{ (r33)}$$
$$H_2NNH_3* + * \rightarrow NH_2* + NH_3* \text{ (r34)}$$

Transition states found for these reactions are presented in **Fig. 10.** From H_XNNH_Y dissociation energy barriers obtained explicitly here, we derived scaling relationships to infer energy barriers from reaction energies for the same reaction on different metals (**Fig. S26**).

We found the first hydrogenation of N_2* to NNH* to already significantly facilitate N-N bond breaking. For instance, while the N_2* dissociation barrier for Ni was estimated to be 2.57 eV, the NNH* dissociation barrier on this metal was found to be 0.45 eV. Thus, the barrier for *r27* was estimated to range between 0.00 eV in Fe to 3.00 eV in Ag. This trend for *r27* is consistent with general trends for *r28-r34*, whose barriers tended to be lower the more nitrophilic

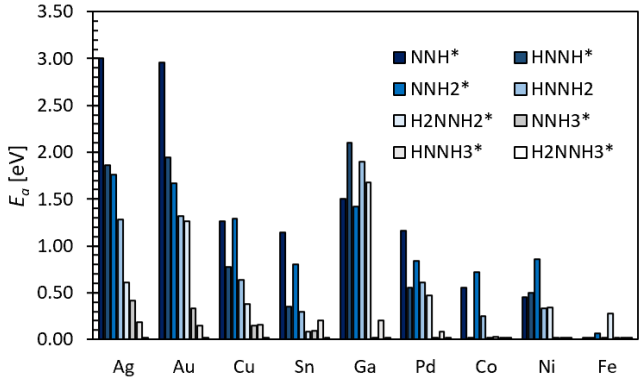

Figure 11. Energy barriers for the dissociation of H_XNNH_Y species on studied metal surfaces. For each metal, *Y* increases from left to right (and for same *Y*, larger *X* is placed to the right). Note that 0.00 eV bars were given a 0.02 eV height to facilitate visualization.

the metal was (**Fig. 11**). For instance, on Fe, all H_XNNH_Y species dissociate with barriers below 0.5 eV, whereas on Ag, only until hydrogenation creates NNH_3, does the barrier to break the N-N bond goes below 0.5 eV. Accordingly, under the assumption of one third entropy loss (**Table 2**) on a highly nitrophilic metal such as Fe one can expect dissociation to occur as early as NNH* is formed, with hydrogenation continuing on N* and NH*. On the other hand, following the sequence on **Fig. 9**, on a metal such as Ag, hydrogenation could continue until H_2NNH_3 is formed, at which point dissociation can occur, releasing an NH_3* and the NH_2 being hydrogenated in a subsequent step. To be sure, if the radical actually loses more entropy at the transition states for ER hydrogenations, N_2H_Y dissociation reactions would become more competitive in more metals, and earlier in the hydrogenation sequence. For instance, N_2H_Y dissociation barriers in Co and Ni are all below 1.0 eV, which is the threshold we noted for competitivity in case the radical loses two thirds of its entropy.

As inferred from the statements above, an observed general trend is that, as hydrogenation increases, N-N bond breaking tends to become easier. Although the hydrogenation of a given N atom is more influential than the overall hydrogenation of the H_XNNH_Y species. For instance, the barrier for NNH_3* dissociation is lower than for $HNNH_2$* dissociation. This trend is more apparent on the less nitrophilic metals. Ga, a moderately nitrophilic metal, is intriguing in that dissociation barriers of H_XNNH_Y species tend to remain above 1.0 eV as long as *Y* stays below 3. Once *Y* equals 3, the dissociation barrier drops dramatically, at least below 0.2 eV. In this aspect, it is quite different than the slightly less nitrophilic Sn, on which the dissociation of H_XNNH_Y species seems to be dramatically easier.

LH reactions.

Hydrogenation. Under the accepted mechanism for the HB process, hydrogenation occurs through the LH reactions:

$$N^* + H^* \rightarrow NH^* \text{ (r35)}$$
$$NH^* + H^* \rightarrow NH_2^* \text{ (r36)}$$
$$NH_2^* + H^* \rightarrow NH_3^* \text{ (r37)}$$

Calculated reaction energies for these reactions are shown in **Fig. 12**, along with hydrogenation barriers estimated from scaling relationships using our calculated reaction energies as input. Reactions *r35-r37* tend toward exothermicity and

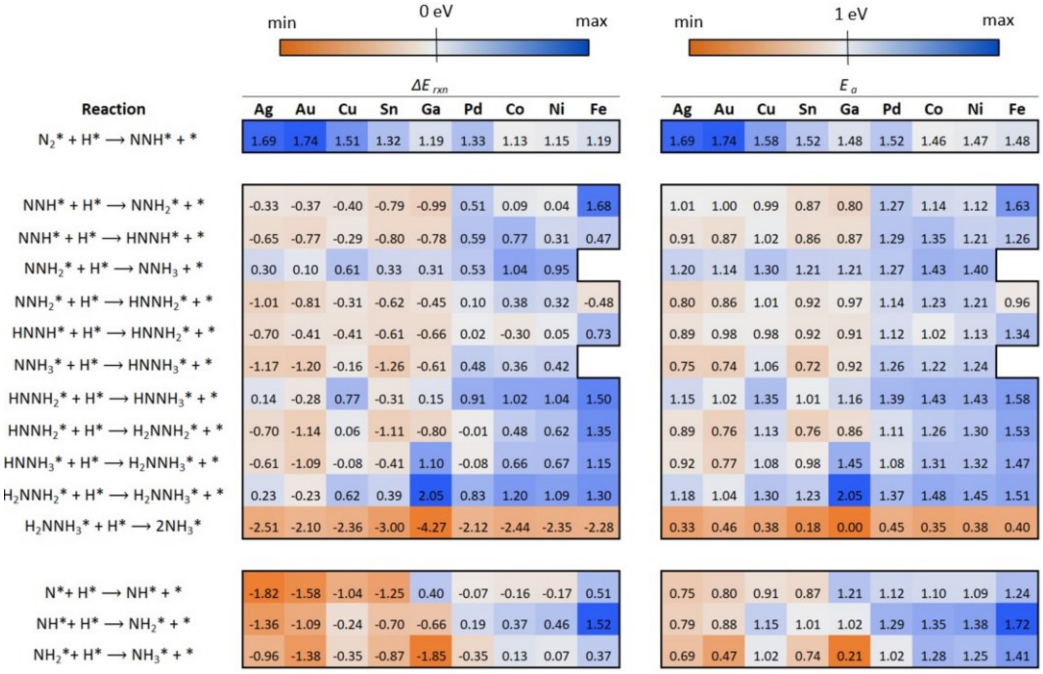

Reaction	Ag	Au	Cu	Sn	Ga	Pd	Co	Ni	Fe	Ag	Au	Cu	Sn	Ga	Pd	Co	Ni	Fe
$N_2^* + H^* \rightarrow NNH^* + *$	1.69	1.74	1.51	1.32	1.19	1.33	1.13	1.15	1.19	1.69	1.74	1.58	1.52	1.48	1.52	1.46	1.47	1.48
$NNH^* + H^* \rightarrow NNH_2^* + *$	-0.33	-0.37	-0.40	-0.79	-0.99	0.51	0.09	0.04	1.68	1.01	1.00	0.99	0.87	0.80	1.27	1.14	1.12	1.63
$NNH^* + H^* \rightarrow HNNH^* + *$	-0.65	-0.77	-0.29	-0.80	-0.78	0.59	0.77	0.31	0.47	0.91	0.87	1.02	0.86	0.87	1.29	1.35	1.21	1.26
$NNH_2^* + H^* \rightarrow NNH_3 + *$	0.30	0.10	0.61	0.33	0.31	0.53	1.04	0.95		1.20	1.14	1.30	1.21	1.21	1.27	1.43	1.40	
$NNH_2^* + H^* \rightarrow HNNH_2^* + *$	-1.01	-0.81	-0.31	-0.62	-0.45	0.10	0.38	0.32	-0.48	0.80	0.86	1.01	0.92	0.97	1.14	1.23	1.21	0.96
$HNNH^* + H^* \rightarrow HNNH_2^* + *$	-0.70	-0.41	-0.41	-0.61	-0.66	0.02	-0.30	0.05	0.73	0.89	0.98	0.98	0.92	0.91	1.12	1.02	1.13	1.34
$NNH_3^* + H^* \rightarrow HNNH_3^* + *$	-1.17	-1.20	-0.16	-1.26	-0.61	0.48	0.36	0.42		0.75	0.74	1.06	0.72	0.92	1.26	1.22	1.24	
$HNNH_2^* + H^* \rightarrow HNNH_3^* + *$	0.14	-0.28	0.77	-0.31	0.15	0.91	1.02	1.04	1.50	1.15	1.02	1.35	1.01	1.16	1.39	1.43	1.43	1.58
$HNNH_2^* + H^* \rightarrow H_2NNH_2^* + *$	-0.70	-1.14	0.06	-1.11	-0.80	-0.01	0.48	0.62	1.35	0.89	0.76	1.13	0.76	0.86	1.11	1.26	1.30	1.53
$HNNH_3^* + H^* \rightarrow H_2NNH_3^* + *$	-0.61	-1.09	-0.08	-0.41	1.10	-0.08	0.66	0.67	1.15	0.92	0.77	1.08	0.98	1.45	1.08	1.31	1.32	1.47
$H_2NNH_2^* + H^* \rightarrow H_2NNH_3^* + *$	0.23	-0.23	0.62	0.39	2.05	0.83	1.20	1.09	1.30	1.18	1.04	1.30	1.23	2.05	1.37	1.48	1.45	1.51
$H_2NNH_3^* + H^* \rightarrow 2NH_3^*$	-2.51	-2.10	-2.36	-3.00	-4.27	-2.12	-2.44	-2.35	-2.28	0.33	0.46	0.38	0.18	0.00	0.45	0.35	0.38	0.40
$N^* + H^* \rightarrow NH^* + *$	-1.82	-1.58	-1.04	-1.25	0.40	-0.07	-0.16	-0.17	0.51	0.75	0.80	0.91	0.87	1.21	1.12	1.10	1.09	1.24
$NH^* + H^* \rightarrow NH_2^* + *$	-1.36	-1.09	-0.24	-0.70	-0.66	0.19	0.37	0.46	1.52	0.79	0.88	1.15	1.01	1.02	1.29	1.35	1.38	1.72
$NH_2^* + H^* \rightarrow NH_3^* + *$	-0.96	-1.38	-0.35	-0.87	-1.85	-0.35	0.13	0.07	0.37	0.69	0.47	1.02	0.74	0.21	1.02	1.28	1.25	1.41

Figure 12. Reaction (ΔE_{rxn}) and activation (E_a) energies for LH hydrogenation reactions. Color scale for ΔE_{rxn} and E_a indicated by the top color bars. Orange and blue indicate more favorable and less favorable reactions, respectively.

lower barrier as metal nitrophilicity decreases. Indeed, the barriers for *r35-r37* tend to be below 1.00 eV for Sn, Cu, Au and Ag (but still above 0.5 eV), and above 1.00 eV for Fe, Ni, Co, and Pd (with Ga straddling both groups). Thus, only for the former group LH hydrogenation would have a chance to be competitive with ER hydrogenation under the assumption of either one third or two thirds entropy loss by the radical in the latter reactions (TS_a ~ 0.5 eV and TS_a ~ 1.0 eV, respectively).

As noted from our discussion on ER reactions, formation of NNH can initiate the associative mechanism. An alternative to the ER pathway would be NNH formation through the LH hydrogenation reaction:

$$N_2^* + H^* \rightarrow NNH^* \text{ (r38)}$$

However, using a universal scaling relationship[48], we estimate barriers of 1.46 eV or higher for *r38* (**Fig. 12**). Thus, based on the entropic barriers (**Table 2**) for the NNH-forming ER reactions *r5* and *r6,* it is likely that NNH formation is dominated by ER pathways.

Once NNH is formed, then hydrogenation could occur through the LH reactions:

$$NNH^* + H^* \rightarrow NNH_2^* \text{ (r39)}$$
$$NNH^* + H^* \rightarrow HNNH^* \text{ (r40)}$$
$$NNH_2^* + H^* \rightarrow NNH_3^* \text{ (r41)}$$
$$NNH_2^* + H^* \rightarrow HNNH_2^* \text{ (r42)}$$

$$HNNH^* + H^* \rightarrow HNNH_2^* \quad (r43)$$
$$NNH_3^* + H^* \rightarrow HNNH_3^* \quad (r44)$$
$$HNNH_2^* + H^* \rightarrow HNNH_3^* \quad (r45)$$
$$HNNH_2^* + H^* \rightarrow H_2NNH_2^* \quad (r46)$$
$$HNNH_3^* + H^* \rightarrow H_2NNH_3^* \quad (r47)$$
$$H_2NNH_2^* + H^* \rightarrow H_2NNH_3^* \quad (r48)$$
$$H_2NNH_3^* + H^* \rightarrow 2NH_3^* \quad (r49)$$

Similar to *r35-r37*, **Fig. 12** shows that *r39-r48* tend more toward exothermicity and barriers below 1.00 eV on Sn, Cu, Au and Ag and toward endothermicity and barriers above 1.00 eV on Fe, Ni, Co, and Pd (with Ga straddling both groups). The reaction with a commonly low barrier is *r49,* which occurs with a barrier lower than 0.50 eV on all metals. As for the least resistant LH hydrogenation path, for both the least nitrophilic metals in the former group, Ag and Au, with the most nitrophilic metal in the latter group, Fe, the least resistant path to arrive to $H_2NNH_3^*$ is via *r40* → *r43* → *r46* → *r48*. For Ag and Au the highest barrier to be overcome is 1.18 eV, 1.04 eV, and 1.30 eV, whereas for Fe is 1.53 eV. For the remaining metals, the least resistance hydrogenation sequence is *r39* → *r42* → *r46* → *r48*, where the lowest barrier to be overcome is 0.8 eV. Comparing the barriers between LH and ER hydrogenation, it is likely that when radical concentration is above some critical value ER hydrogenation dominates, at least until H_2NNH_3 is formed. Once the latter species is formed, the low barrier for *r49* may make NH_3^* formation via a last LH step competitive with a last ER step.

Recombination. Alternatives to recombination ER reactions *r9* and *r10* are LH reactions *r11* and *r12:*

$$2N^* \rightarrow N_{2(g)} + 2^* \quad (r50)$$
$$2H^* \rightarrow H_{2(g)} + 2^* \quad (r51)$$

but in contrast to the ER route, these reactions do present an energy barrier and tend to be more favorable for hydrogen (E_a ranging from 0.48 eV on Sn to 1.18 eV on Pd) than for nitrogen recombination (E_a ranging from 1.10 eV on Ag to 3.29 eV on Fe) (**Table S8**). Similar to ER recombination, LH recombination of nitrogen and hydrogen correlates inversely with the adsorption strength of N* and H*, respectively. The barriers for LH recombination of nitrogen suggest it as unlikely to be competitive with ER nitrogen recombination in any metal. On the other hand, LH recombination of hydrogen could be competitive with the analogous ER reaction on Ga, Sn, Ag, and Au.

Adsorption and desorption reactions. The (negative of) adsorption energies discussed in **Section 3.2**. can be considered as the reaction energies for (desorption) adsorption reactions of species that can be found in the plasma phase as molecules or radicals. For instance, adsorption energies for N* and NH* can be considered reaction energies for the adsorption of N• and NH• radicals, respectively, whereas the negative of the adsorption energies for NH_3^*, $N_2H_2^*$ and $N_2H_4^*$ can be considered reaction energies for the desorption

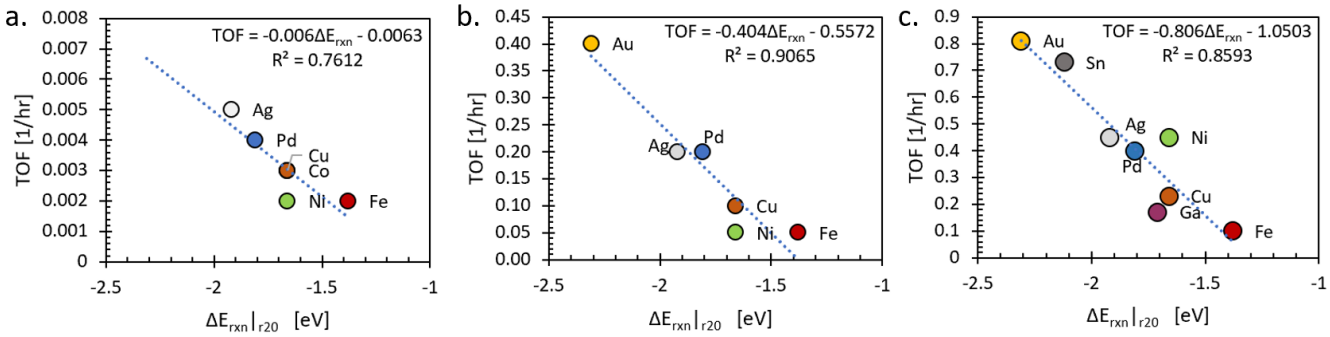

Figure 13. Correlation between turnover frequency (TOF) in various experiments and reaction energy for *r20* (H• + HNNH2* → $HNNH_3^*$). a) Current experiments: DBD reactor, T =125 C, P = 1 atm, N_2:H_2 ratio= 1, flow rate = 25 sccm, plasma power = 15W, b) DBD reactor, T = not reported (no heat exchange), P = 1 atm, N_2:H_2 ratio= 1, flow rate = 100 sccm, applied voltage = 5 kV, taken from ref.[36], c) RF reactor, T = 400 C, P = 3.5 x 10^{-4} atm, N_2:H_2 ratio= 0.25, flow rate = 20 sccm, plasma power = 300 W, taken from ref [20].

of $NH_{3(g)}$, $N_2H_{2(g)}$ and $N_2H_{4(g)}$, respectively. The adsorption of radicals is highly exothermic, meaning their desorption is highly endothermic. On the other hand, to what extent molecular species are likely to desorb before they continue to react may depending on the metal. For example, HNNH (diazene) on Fe is less likely to desorb (ΔE_{des} = 3.12 eV) before it dissociates (E_a = 0.00 eV), whereas on Sn, Au or Ag (ΔE_{des} < 0.65 eV) this desorption may be more competitive with, say, ER hydrogenation to $HNNH_2$. H_2NNH_2 (hydrazine) desorption is somewhat less competitive with ER hydrogenation, with slightly higher barriers even on Ag (ΔE_{des} > 0.65 eV).

Correlations with experiments. As previously noted, the reaction energetics presented here can be used to build DFT-informed kinetic models for each metal. The complexity of the reaction networks makes it apparent that these models are necessary to fully shed light on the dominant reaction pathways as a function of reaction conditions (which affect plasma composition) and implications on relative metal performance. However, at this point we can already note that the plausible dominance of ER reactions discussed here based on DFT calculations is consistent with the lesser impact of metal composition on plasma-assisted ammonia synthesis[20,27,36] compared to the thermocatalytic process, for which observed TOF across metals span a wide range of orders of magnitude.[64]

Full understanding of the plasma-assisted ammonia synthesis mechanism (and plasma catalysts interactions) can open the door to rational manipulation of plasma conditions

(reactor design) to maximize ammonia production as well as to identification of better catalysts than currently tested. The latter typically relies on the identification of a rate controlling step (RCS)[65], with catalyst modifications rationalized on the basis of boosting the RCS. Knowledge of the RSC can also facilitate computational high throughput screening using a "cheap" catalyst descriptor associated with the RCS (typically a binding energy) ref.[66,67] However, given the breadth of reaction energetics data herein presented, we considered the empirical identification of a potential *ad hoc* descriptor that could already be used for screening.

To accomplish this, we first calculated TOFs from catalytic tests in an atmospheric pressure DBD reactor (see **Section 2.1**). Fe, Ni, Co, Pd, Cu and Ag were tested, with ammonia synthesis rates R_{NH3} varying from 2.3 μmol_{NH3}/min in Fe to 4.5 μmol_{NH3}/min in Au (with energy yields varying from 0.15 gNH_3/kWh to 0.30 gNH_3/kWh, respectively). A common observation to our current experiments and those earlier by us (RF)[20] and Iwamoto et al.[36] (DBD) is that an HB-inactive metal such as Ag is found to outperform an HB-active metals such as Fe.

Calculating exact values for experimental TOFs is one of the most difficult endeavors in catalysis due to uncertainties on what the active site are and on their quantification. However, for the exercise here, we are only interested in trends across metals. Thus, to calculate TOFs we did not attempt to subtract the background NH_3 production in the absence of catalyst (as it would be the subtract the same number to all metals) and approximated *all* metal atoms as active sites, with which:

$$TOF = \frac{R_{NH_3}}{n_{metal}} \quad (7)$$

where n_{metal} is the number of moles of the metal estimated from the metal molecular weight and the mass of the metal electrodes (Fe = 4.3 g, Ni = 4.5 g, Co = 4.7 g, Pd = 5.9 g, Cu = 4.8 g, Ag = 5.3 g). This approach is consistent with our estimation of TOFs for our earlier ammonia synthesis experiments on an RF reactor, which we also examine here. Additionally, this approach allows us to take advantage of data by Iwamoto et al.[36] who tested a breadth of metal catalysts to convert their rate data to TOFs to further test descriptors. Indeed, given the variability of plasma conditions that can be tested for ammonia synthesis, we aimed to identify a descriptor that could potentially be robust to changing reaction conditions.

Earlier, Iwamoto et al.[36] correlated *reaction rates* with M_3N formation energy, which was calculated essentially as N* adsorption energy on a M_3 cluster. Thus, we first tested the reaction energy for:

$$N\bullet + * \rightarrow N* \qquad (r52)$$

as a possible descriptor. The correlation (R^2) between TOFs and this descriptor was 0.59 for Iwamoto et al TOFs and 0.73 for TOFs herein but decreased to 0.38 for TOFs in our RF experiments. Given that we observed a strong correlation (R^2 =0.89) between NH intensity from the OES and TOFs herein (**Fig. S28**), we considered also the reaction energy for:

$$NH\bullet + * \rightarrow NH* \qquad (r53)$$

as descriptor, but a similar scenario to that for ΔE_{rxn} of *r52* occurred. At this point, we decided to test all the reaction energies at our disposal as potential descriptor and calculated their correlation factors with the above TOFs (**Fig. S29**). Through this exercise, we identified ΔE_{rxn} of *r20* as a robust descriptor for TOFs herein (R^2 = 0.76), TOFs for Iwamoto et al. (R^2 = 0.91), and TOFs for our earlier RF experiments (R^2 = 0.86) as shown in **Fig. 13**. Note that the lower R^2 for **Fig. 13a** is likely due to the absence of Au, as dropping Au from **Fig. 13b,c** results in R^2 values similar to **Fig. 13a**.

Intriguingly, *r20* is an ER hydrogenation reaction, which is a type of reaction we have shown is likely important for plasma-assisted NH_3 synthesis. But *r20* is a hydrogenation step ($HNNH_2$ to $HNNH_3$) that is less favorable than the competing hydrogenation step *r21* ($HNNH_2$ to H_2NNH_2). Without info from a kinetic model, we ascribe this to the empirical character of the descriptor. As a side note, ΔE_{rxn} of *r21* correlates with R^2 in the 0.71 - 0.80 range for the TOFs in **Fig. 13**. In any case, it is important to note that the empiric character of the descriptor herein identified does not preclude its potential effectiveness in catalyst screening. Also, note that since we know the electrode area in our experiments (9.6 x 10^{-4} m2), we could have presented TOFs based on these areas, which are identical for all electrodes. Such exercise, produces a higher r^2 (r^2= 0.88, **Fig. S30**) than in **Fig. 13a**, but does not allow us to compare fairly with the data in **Fig. 13b-c.**

■ CONCLUSIONS

In consistency with growing literature, optical emission spectroscopy in a DBD reactor were consistent/suggestive with/of the presence of plasma radicals during catalytic, plasma-assisted ammonia synthesis, but likely at much higher concentrations that non-dissociated N_2 species (which could include vibrationally excited N_2). Comparison of OES also suggested that the effect of the metal on the plasma, while statistically significant, was weak. All the above motivated comprehensive DFT calculations to understand the favorability of new reactions (i.e., not occurring during the traditional Haber-Bosch process) that could be facilitated by these species. These calculations were performed on nine metals, with the obtained energetics being of potential use in kinetics models that could yield a more accurate picture of the dominant pathways within the complex reaction network of this process. However, the scope of the work here was set to achieving a more granular analysis of the relative (energy-based) favorability of proposed reactions, and changes in this favorability across metals. This analysis was found to be suggestive of i) the plausibility of an associative pathway initiated by NNH formation from radical-involving reactions, ii) the likelihood of N radicals as the dominant source of N*, iii) the probability of ER hydrogenation to be the dominant hydrogenation pathway, and iv) the likelihood of difference in dominant pathways across metals when doing plasma-assisted ammonia synthesis. Note, however, that our analysis here is based on a "transition state theory" approach, and important points such as energy dissipation during highly exothermic reactions involving impinging radicals were not considered in this work. Finally, the breadth of energetics data, along with catalytic experiments on six metals on a DBD reactor, allowed us to empirically identify a potentially robust (and easy to calculate)

energetic descriptor (the reaction energy for $HNNH_2$ ER hydrogenation to $HNNH_3$) to discover better catalysts for these application via computational screening.

SUPPLEMENTARY INFORMATION

Electronic Supplementary Information (ESI) available: Complementary optical emission spectra. Complementary snapshots of optimized reactant, product and transition state geometries. Scaling relationships. Tabulated reaction energetics data. R^2 for correlation of TOFs with different reaction energies.

AUTHOR INFORMATION

Corresponding Author

* dgomezgualdron@mines.edu

Funding Sources

National Science Foundation, CBET.

ACKNOWLEDGMENTS

D.A.G.-G. and M.L.C. acknowledge funding from collaborative NSF grants CBET 1921484 and CBET 1947303, respectively. Simulations were made possible by the Mio supercomputer cluster at Colorado School of Mines and NERSC computational resources from the U.S. Department of Energy (DOE). The authors thank Oscar Bender-Stone for his analysis of correlations between experimental TOF data and DFT-calculated reaction energies. Mr. Bender-Stone participated in this project through the Jefferson County Executive High School Internship Program.

REFERENCES

(1) Sutton, M. A.; Erisman, J. W.; Dentener, F.; Möller, D. Ammonia in the environment: from ancient times to the present. *Environ. Pollut.* **2008**, *156* (3), 583–604.

(2) Giddey, S.; Badwal, S. P. S.; Munnings, C.; Dolan, M. Ammonia as a renewable energy transportation media. *ACS Sustain. Chem. Eng.* **2017**, *5* (11), 10231–10239.

(3) Crabtree, G. W.; Dresselhaus, M. S.; Buchanan, M. V. The Hydrogen Economy. *Phys. Today* **2004**, *57* (12), 39–44.

(4) Ghavam, S.; Vahdati, M.; Wilson, I. A. G.; Styring, P. Sustainable ammonia production processes. *Front. Energy Res.* **2021**, *9* (2021: 34).

(5) Smith, C.; Hill, A. K.; Torrente-Murciano, L. Current and future role of Haber–Bosch ammonia in a carbon-free energy landscape. *Energy Environ. Sci.* **2020**, *13* (2), 331–344.

(6) Li, C.; Wang, T.; Gong, J. Alternative strategies toward sustainable ammonia synthesis. *Trans. Tianjin Univ.* **2020**, *26* (2), 67–91.

(7) Carreon, M. L. Plasma catalytic ammonia synthesis: state of the art and future directions. *J. Phys. D, Appl. Phys.* **2019**, *52* (48), 483001.

(8) Han, G.-F.; Li, F.; Chen, Z.-W.; Coppex, C.; Kim, S.-J.; Noh, H.-J.; Fu, Z.; Lu, Y.; Singh, C. V.; Siahrostami, S.; et al. Mechanochemistry for ammonia synthesis under mild conditions. *Nat. Nanotechnol.* **2021**, *16* (3), 325–330.

(9) Zhang, Z.; Way, J. D.; Wolden, C. A. Design and operational considerations of catalytic membrane reactors for ammonia synthesis. *AIChE J.* **2021**, *67* (8).

(10) Montoya, J. H.; Tsai, C.; Vojvodic, A.; Nørskov, J. K. The challenge of electrochemical ammonia synthesis: A new perspective on the role of nitrogen scaling relations. *ChemSusChem* **2015**, *8* (13), 2180–2186.

(11) Murakami, K.; Tanaka, Y.; Sakai, R.; Toko, K.; Ito, K.; Ishikawa, A.; Higo, T.; Yabe, T.; Ogo, S.; Ikeda, M.; et al. The important role of N2H formation energy for low-temperature ammonia synthesis in an electric field. *Catal. Today 351 (2020): 119-124*.

(12) Singh, A. R.; Rohr, B. A.; Schwalbe, J. A.; Cargnello, M.; Chan, K.; Jaramillo, T. F.; Chorkendorff, I.; Nørskov, J. K. Electrochemical ammonia synthesis—the selectivity challenge. *ACS Catal.* **2017**, *7* (1), 706–709.

(13) Carreon, M. L. Plasma catalysis: a brief tutorial. *Plasma Res. Express* **2019**, *1* (4), 043001.

(14) Fu, R.; Feldman, D.; Margolis, R.; Woodhouse, M.; Ardani, K. *U.S. solar photovoltaic system cost benchmark: Q1 2017*; EERE Publication and Product Library, 2017.

(15) Zeng, Z.; Ziegler, A. D.; Searchinger, T.; Yang, L.; Chen, A.; Ju, K.; Piao, S.; Li, L. Z. X.; Ciais, P.; Chen, D.; et al. A reversal in global terrestrial stilling and its implications for wind energy production. *Nat. Clim. Chang.* **2019**, *9* (12), 979–985.

(16) van Helden, J. H.; Wagemans, W.; Yagci, G.; Zijlmans, R. A. B.; Schram, D. C.; Engeln, R.; Lombardi, G.; Stancu, G. D.; Röpcke, J. Detailed study of the plasma-activated catalytic generation of ammonia in N2-H2 plasmas. *J. Appl. Phys.* **2007**, *101* (4), 043305.

(17) Shah, J.; Wang, W.; Bogaerts, A.; Carreon, M. L. Ammonia synthesis by radio frequency plasma catalysis: revealing the underlying mechanisms. *ACS Appl. Energy Mater.* **2018**, *1* (9), 4824–4839.

(18) Kiyooka, H.; Matsumoto, O. Reaction scheme of ammonia synthesis in the ECR plasmas. *Plasma Chem. Plasma Process.* **1996**, *16* (4), 547–562.

(19) Tanaka, S.; Uyama, H.; Matsumoto, O. Synergistic effects of catalysts and plasmas on the synthesis of ammonia and hydrazine. *Plasma Chem. Plasma Process.* **1994**, *14* (4), 491–504.

(20) Shah, J.; Gorky, F.; Psarras, P.; Seong, B.; Gómez-Gualdrón, D. A.; Carreon, M. L. Enhancement of the Yield of Ammonia by Hydrogen-Sink Effect during Plasma Catalysis. *ChemCatChem 12.4 (2020): 1200-1211*.

(21) Neyts, E. C.; Bogaerts, A. Understanding plasma catalysis through modelling and simulation—a review. *J. Phys. D, Appl. Phys.* **2014**, *47* (22), 224010.

(22) Kim, H.-H.; Teramoto, Y.; Ogata, A.; Takagi, H.; Nanba, T. Atmospheric-pressure nonthermal plasma synthesis of

ammonia over ruthenium catalysts. *Plasma Process Polym* **2017**, *14* (6), 1600157.

(23) Barboun, P. M.; Mehta, P.; Herrera, F.; Go, D. B.; Schneider, W. F.; Hicks, J. C. Distinguishing Plasma Contributions to Catalyst Performance in Plasma-Assisted Ammonia Synthesis. *ACS Sustain. Chem. Eng.* **2019**, *7* (9), 8621–8630.

(24) Rouwenhorst, K. H. R.; Kim, H.-H.; Lefferts, L. Vibrationally Excited Activation of N_2 in Plasma-Enhanced Catalytic Ammonia Synthesis: A Kinetic Analysis. *ACS Sustain. Chem. Eng.* **2019**, *7* (20), 17515–17522.

(25) Rouwenhorst, K. H. R.; Burbach, H. G. B.; Vogel, D. W.; Núñez Paulí, J.; Geerdink, B.; Lefferts, L. Plasma-catalytic ammonia synthesis beyond thermal equilibrium on Ru-based catalysts in non-thermal plasma. *Catal. Sci. Technol.* **2021**, *11* (8), 2834–2843.

(26) Mehta, P.; Barboun, P. M.; Engelmann, Y.; Go, D. B.; Bogaerts, A.; Schneider, W. F.; Hicks, J. C. Plasma-Catalytic Ammonia Synthesis beyond the Equilibrium Limit. *ACS Catal.* **2020**, *10* (12), 6726–6734.

(27) Mehta, P.; Barboun, P.; Herrera, F. A.; Kim, J.; Rumbach, P.; Go, D. B.; Hicks, J. C.; Schneider, W. F. Overcoming ammonia synthesis scaling relations with plasma-enabled catalysis. *Nat. Catal. 1.4 (2018): 269-275*.

(28) Wang, Y.; Craven, M.; Yu, X.; Ding, J.; Bryant, P.; Huang, J.; Tu, X. Plasma-Enhanced Catalytic Synthesis of Ammonia over a Ni/Al2O3 Catalyst at Near-Room Temperature: Insights into the Importance of the Catalyst Surface on the Reaction Mechanism. *ACS Catal.* **2019**, *9* (12), 10780–10793.

(29) Navascués, P.; Obrero-Pérez, J. M.; Cotrino, J.; González-Elipe, A. R.; Gómez-Ramírez, A. Unraveling Discharge and Surface Mechanisms in Plasma-Assisted Ammonia Reactions. *ACS Sustain. Chem. Eng.* **2020**, *8* (39), 14855–14866.

(30) Winter, L. R.; Ashford, B.; Hong, J.; Murphy, A. B.; Chen, J. G. Identifying surface reaction intermediates in plasma catalytic ammonia synthesis. *ACS Catal.* **2020**, *10* (24), 14763–14774.

(31) Zhao, H.; Song, G.; Chen, Z.; Yang, X.; Yan, C.; Abe, S.; Ju, Y.; Sundaresan, S.; Koel, B. E. *In Situ* Identification of NNH and N_2 H_2 by Using Molecular-Beam Mass Spectrometry in Plasma-Assisted Catalysis for NH_3 Synthesis. *ACS Energy Lett.* **2021**, 53–58.

(32) Yamijala, S. S. R. K. C.; Nava, G.; Ali, Z. A.; Beretta, D.; Wong, B. M.; Mangolini, L. Harnessing Plasma Environments for Ammonia Catalysis: Mechanistic Insights from Experiments and Large-Scale Ab Initio Molecular Dynamics. *J. Phys. Chem. Lett.* **2020**, *11* (24), 10469–10475.

(33) van 't Veer, K.; Engelmann, Y.; Reniers, F.; Bogaerts, A. Plasma-Catalytic Ammonia Synthesis in a DBD Plasma: Role of Microdischarges and Their Afterglows. *J. Phys. Chem. C* **2020**, *124* (42), 22871–22883.

(34) Hong, J.; Pancheshnyi, S.; Tam, E.; Lowke, J. J.; Prawer, S.; Murphy, A. B. Kinetic modelling of NH_3 production in N_2 –H_2 non-equilibrium atmospheric-pressure plasma catalysis. *J. Phys. D, Appl. Phys.* **2017**, *50* (15), 154005.

(35) Carrasco, E.; Jiménez-Redondo, M.; Tanarro, I.; Herrero, V. J. Neutral and ion chemistry in low pressure dc plasmas of H2/N2 mixtures: routes for the efficient production of NH3 and NH4(+). *Phys. Chem. Chem. Phys.* **2011**, *13* (43), 19561–19572.

(36) Iwamoto, M.; Akiyama, M.; Aihara, K.; Deguchi, T. Ammonia Synthesis on Wool-Like Au, Pt, Pd, Ag, or Cu Electrode Catalysts in Nonthermal Atmospheric-Pressure Plasma of N_2 and H_2. *ACS Catal.* **2017**, *7* (10), 6924–6929.

(37) Kresse, G.; Hafner, J. *Ab initio* molecular-dynamics simulation of the liquid-metal–amorphous-semiconductor transition in germanium. *Phys. Rev. B* **1994**, *49* (20), 14251–14269.

(38) Kresse, G.; Hafner, J. *Ab initio* molecular dynamics for liquid metals. *Phys. Rev. B* **1993**, *47* (1), 558–561.

(39) Kresse, G.; Furthmüller, J. Efficiency of ab-initio total energy calculations for metals and semiconductors using a plane-wave basis set. *Comp. Mater. Sci.* **1996**, *6* (1), 15–50.

(40) Perdew, J. P.; Burke, K.; Ernzerhof, M. Generalized gradient approximation made simple. *Phys. Rev. Lett.* **1996**, *77* (18), 3865–3868.

(41) Bučko, T.; Hafner, J.; Lebègue, S.; Ángyán, J. G. Improved description of the structure of molecular and layered crystals: ab initio DFT calculations with van der Waals corrections. *J. Phys. Chem. A* **2010**, *114* (43), 11814–11824.

(42) Grimme, S. Semiempirical GGA-type density functional constructed with a long-range dispersion correction. *J. Comput. Chem.* **2006**, *27* (15), 1787–1799.

(43) Kerber, T.; Sierka, M.; Sauer, J. Application of semiempirical long-range dispersion corrections to periodic systems in density functional theory. *J. Comput. Chem.* **2008**, *29* (13), 2088–2097.

(44) Methfessel, M.; Paxton, A. T. High-precision sampling for Brillouin-zone integration in metals. *Phys. Rev. B* **1989**, *40* (6), 3616–3621.

(45) BIOVIA, Dassault Systèmes, [Materials Studio], [2017], San Diego: Dassault Systèmes, [2021].

(46) Henkelman, G.; Uberuaga, B. P.; Jónsson, H. A climbing image nudged elastic band method for finding saddle points and minimum energy paths. *J. Chem. Phys.* **2000**, *113* (22), 9901–9904.

(47) Henkelman, G.; Jónsson, H. A dimer method for finding saddle points on high dimensional potential surfaces using only first derivatives. *J. Chem. Phys.* **1999**, *111* (15), 7010–7022.

(48) Wang, S.; Petzold, V.; Tripkovic, V.; Kleis, J.; Howalt, J. G.; Skúlason, E.; Fernández, E. M.; Hvolbæk, B.; Jones, G.; Toftelund, A.; et al. Universal transition state scaling relations for (de)hydrogenation over transition metals. *Phys. Chem. Chem. Phys.* **2011**, *13* (46), 20760–20765.

(49) Herrera, F. A.; Brown, G. H.; Barboun, P.; Turan, N.; Mehta, P.; Schneider, W. F.; Hicks, J. C.; Go, D. B. The impact of transition metal catalysts on macroscopic dielectric barrier discharge (DBD) characteristics in an ammonia synthesis plasma catalysis reactor. *J. Phys. D, Appl. Phys.* **2019**, *52* (22), 224002.

(50) Medford, A. J.; Vojvodic, A.; Hummelshøj, J. S.; Voss, J.; Abild-Pedersen, F.; Studt, F.; Bligaard, T.; Nilsson, A.; Nørskov, J. K. From the Sabatier principle to a predictive theory of transition-metal heterogeneous catalysis. *J. Catal.* **2015**, *328*, 36–42.

(51) Abild-Pedersen, F.; Greeley, J.; Studt, F.; Rossmeisl, J.; Munter, T. R.; Moses, P. G.; Skúlason, E.; Bligaard, T.; Nørskov, J. K. Scaling properties of adsorption energies for hydrogen-containing molecules on transition-metal surfaces. *Phys. Rev. Lett.* **2007**, *99* (1), 016105.

(52) Santiago-Rodríguez, Y.; Herron, J. A.; Curet-Arana, M. C.; Mavrikakis, M. Atomic and molecular adsorption on Au(111). *Surf Sci* **2014**, *627*, 57–69.

(53) Xu, L.; Lin, J.; Bai, Y.; Mavrikakis, M. Atomic and molecular adsorption on cu(111). *Top. Catal.* **2018**, *61* (9-11), 736–750.

(54) Herron, J. A.; Tonelli, S.; Mavrikakis, M. Atomic and molecular adsorption on Pd(111). *Surf Sci* **2012**, *606* (21-22), 1670–1679.

(55) Bai, Y.; Kirvassilis, D.; Xu, L.; Mavrikakis, M. Atomic and molecular adsorption on Ni(111). *Surf Sci* **2019**, *679*, 240–253.

(56) Garden, A. L.; Skúlason, E. The mechanism of industrial ammonia synthesis revisited: calculations of the role of the associative mechanism. *J. Phys. Chem. C* **2015**, *119* (47), 26554–26559.

(57) Back, S.; Jung, Y. On the mechanism of electrochemical ammonia synthesis on the Ru catalyst. *Phys. Chem. Chem. Phys.* **2016**, *18* (13), 9161–9166.

(58) Psarras, P.; Anderson, R.; Gómez-Gualdrón, D. A.; Wilcox, J. Material Consequences of Hydrogen Dissolution in Palladium Alloys Observed from First Principles. *J. Phys. Chem. C* **2019**, *123* (36), 22158–22171.

(59) Yeo, S. C.; Han, S. S.; Lee, H. M. Adsorption, dissociation, penetration, and diffusion of N2 on and in bcc Fe: first-principles calculations. *Phys. Chem. Chem. Phys.* **2013**, *15* (14), 5186–5192.

(60) Jiang, D. E.; Carter, E. A. Diffusion of interstitial hydrogen into and through bcc Fe from first principles. *Phys. Rev. B* **2004**, *70* (6), 064102.

(61) Molecular theory of gases and liquids. J. O. Hirschfelder, C. F. Curtiss, and R. B. Bird. Wiley, New York, 1954. xxvi + 1219 pp., $20.00. *J. Polym. Sci.* **1955**, *17* (83), 116–116.

(62) Loenders, B.; Engelmann, Y.; Bogaerts, A. Plasma-Catalytic Partial Oxidation of Methane on Pt(111): A Microkinetic Study on the Role of Different Plasma Species. *J. Phys. Chem. C* **2021**, *125* (5), 2966–2983.

(63) Uyama, H.; Nakamura, T.; Tanaka, S.; Matsumoto, O. Catalytic effect of iron wires on the syntheses of ammonia and hydrazine in a radio-frequency discharge. *Plasma Chem. Plasma Process.* **1993**, *13* (1), 117–131.

(64) Dahl, S.; Logadottir, A.; Jacobsen, C. J. H.; Nørskov, J. K. Electronic factors in catalysis: the volcano curve and the effect of promotion in catalytic ammonia synthesis. *Applied Catalysis A: General* **2001**, *222* (1-2), 19–29.

(65) Campbell, C. T. The degree of rate control: A powerful tool for catalysis research. *ACS Catal.* **2017**, *7* (4), 2770–2779.

(66) ANDERSSON, M.; BLIGAARD, T.; KUSTOV, A.; LARSEN, K.; GREELEY, J.; JOHANNESSEN, T.; CHRISTENSEN, C.; NORSKOV, J. Toward computational screening in heterogeneous catalysis: Pareto-optimal methanation catalysts. *J. Catal.* **2006**, *239* (2), 501–506.

(67) Chen, B. W. J.; Xu, L.; Mavrikakis, M. Computational methods in heterogeneous catalysis. *Chem. Rev.* **2021**, *121* (2), 1007–1048.

TOC Graph